

Bubble Behavior in Subcooled Flow Boiling on Surfaces of Variable Wettability

by

Emily W. Tow

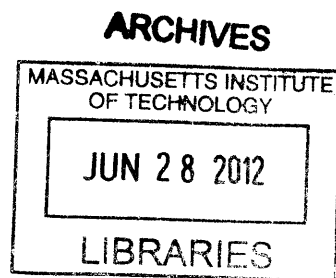
Submitted to the
Department of Mechanical Engineering
in Partial Fulfillment of the Requirements for the Degree of

Bachelor of Science in Mechanical Engineering

at the

Massachusetts Institute of Technology

June 2012



© 2012 Massachusetts Institute of Technology.
All rights reserved.

Signature of Author.....
Department of Mechanical Engineering
May 11, 2012

Certified by.....
Evelyn N. Wang
Associate Professor of Mechanical Engineering
Thesis Supervisor

Accepted by.....
John H. Lienhard V
Samuel C. Collins Professor of Mechanical Engineering
Undergraduate Officer

Bubble Behavior in Subcooled Flow Boiling on Surfaces of Variable Wettability

by

Emily W. Tow

Submitted to the Department of Mechanical Engineering on May 11, 2012
in Partial Fulfillment of the Requirements for the Degree of

Bachelor of Science in Mechanical Engineering

ABSTRACT

Flow boiling is important in energy conversion and thermal management due to its potential for very high heat fluxes. By improving understanding of the conditions leading to bubble departure, surfaces can be designed that increase heat transfer coefficients in flow boiling. Bubbles were visualized during subcooled nucleate flow boiling of water on a surface of variable wettability. Images obtained from the videos were analyzed to find parameters influencing bubble size at departure. A model was developed relating the dimensions of the bubble at departure to its upstream and downstream contact angles based on a rigid-body force balance between momentum and surface tension and assuming a skewed truncated spherical bubble shape. Both experimental and theoretical results predict that bubble width and height decrease with increasing flow speed and that the width increases with the equilibrium contact angle. The model also predicts that the width and height increase with the amount of contact angle hysteresis and that the height increases with equilibrium contact angle, though neither of these trends were clearly demonstrated by the data. Several directions for future research are proposed, including modifications to the model to account for deviations of the bubbles from the assumed geometry and research into the parameters controlling contact angle hysteresis of bubbles in a flow. Additionally, observations support that surfaces with periodically-varying contact angle may prevent film formation and increase the heat transfer coefficients in both film and pool boiling.

Thesis Supervisor: Evelyn Wang

Title: Associate Professor of Mechanical Engineering

ACKNOWLEDGEMENTS

I would like to acknowledge several people whose assistance with this research was indispensable to me. First, I must thank my thesis advisor, Professor Evelyn Wang, who provided critical guidance on my research direction. I would like to thank Siyu Chen for working closely with me and performing contact angle and contaminant analysis, Kuang-Han Chu, Ryan Enright, and Professor TieJun Zhang for their help with the planning and execution of this research, and Rong Xiao and Solomon Adera for teaching me to use the lab equipment. Finally, I would like to thank the Air Force Office of Scientific Research (AFOSR) and Battelle for funding this work.

TABLE OF CONTENTS

Acknowledgements	3
List of Figures	5
List of Tables	6
1. Introduction	7
2. Background	9
3. Methods	17
3.1 Experimental Apparatus	17
3.2 Video Collection	21
3.3 Experimental Parameters	23
3.4 Data Extraction	24
4. Results and Discussion	27
4.1 Bubble Departure	27
4.2 Observations	44
4.3 Evaluation of Experimental Fixture	49
5. Conclusion	57
6. References	59
Appendix I: All Departing Bubbles on Contaminated Surface	60
Appendix II: Image Processing Scripts	63

LIST OF FIGURES

2.1	Regions of film boiling in a vertical tube	11
2.2	Contact angle for liquid-vapor-solid interfaces	12
2.3	Flow-direction rigid-body force balance on a bubble	15
3.1.1	Schematic of the experimental apparatus	17
3.1.2	Sample holder	19
3.1.3	Schematic of channel	20
3.1.4	Thin film gold heater on the back of the surface	21
3.4.1	Series of video frames that indicate the premature departure of a bubble	24
3.4.2	MATLAB script inputs for calculation of channel height, bubble width, and downstream and upstream contact angles	25
3.4.3	MATLAB script inputs for calculation of bubble height for an image with known channel height	26
4.1.1	A bubble before and after departure from the surface	28
4.1.2	Bubbles in a variety of sizes and shapes	28
4.1.3	Downstream contact angle plotted against upstream contact angle	29
4.1.4	Contact angle difference plotted against bubble width	30
4.1.5	Water droplet on the contaminated surface during contact angle measurement	31
4.1.6	Water droplet on a smooth silicon surface during contact angle measurement	31
4.1.7	Contact angle measurements of the contaminated surface	32
4.1.8	Plot of width vs. height for all departing bubbles	33
4.1.9	Bubble width at departure is compared to average contact angle	34
4.1.10	Bubble width is compared to downstream and upstream contact angles	35
4.1.11	Bubble height at departure is compared to average contact angle	36
4.1.12	Bubble height is compared to downstream and upstream contact angles	37
4.1.13	Bubble height is plotted against flow speed	38
4.1.14	Theoretical bubble width is compared to the data	40
4.1.15	Theoretical bubble height is compared to the data	41
4.1.16	Bubbles at the moment before departure with overlays of the assumed bubble shape	42
4.2.1	Bubble wiggling before departure	44

4.2.2	Bubble changing shape rapidly before departure	45
4.2.3	A triangular bubble	46
4.2.4	Consecutive images of a bubble showing a rapid change in shape when jumping over a hydrophilic region	47
4.2.5	Hypothetical surface with periodic variations in wettability	48
4.2.6	Bubble that may be trapped in a small hydrophobic area within a hydrophilic region	49
4.3.1	Examples of clear video stills	50
4.3.2	Examples of unclear video stills	51
4.3.3	Consecutive images of a departing bubble which show that video frame rate should be increased	53
4.3.4	Used plain silicon surface showing visual evidence of contamination	54
4.3.5	An XPS test of the contaminated wafer surface.	55

LIST OF TABLES

3.3.1	An XPS test of the contaminated wafer surface.	22
-------	--	----

1. INTRODUCTION

This work aims to inform the design of microstructured surfaces for higher heat fluxes in flow boiling for applications in thermal energy conversion and thermal management. Flow boiling—and boiling in general—are heat transfer processes of great importance to current technology because of the very high heat transfer coefficients that can be achieved.

High heat fluxes are needed in the thermal management of microprocessors as their transistor density grows. As Gordon Moore predicted in 1965, the number of transistors on individual integrated circuits has roughly doubled every two years [1]. However, the increasing transistor density and number of interconnect layers has increased the heat generation per unit area and therefore the necessary heat flux out of the chip. Recently, finned aluminum or copper heatsinks have become insufficient, and heat pipes in combination with fins have been used to more effectively remove heat. The heat removed from the chip by a heat pipe is limited by the critical heat flux (CHF) of the surface-fluid combination. Currently, most heat pipes use pool boiling to begin heat removal from the chip. However, the heat flux can be increased by increasing the speed of the flow past the heated surface, so flow boiling may be the future of thermal management. Although we do not consider the CHF in flow boiling, similar ideas may be involved in extending the region of nucleate boiling to higher vapor qualities in order to increase the heat flux for a given heater temperature.

Microstructured surfaces that exhibit complete wetting and are rough have been shown to increase the CHF in pool boiling over smooth surfaces [2]. Because flow boiling is directional and the forces governing the departure of the bubbles are different, the effectiveness of the same surfaces is unknown in flow boiling. For this reason, the original goal of this research was to evaluate in flow boiling the same microstructured surfaces that had been so successful in pool boiling. These surfaces consisted of an array of micro-scale pillars which in this case created a superhydrophilic surface. The roughness of the surfaces may also augment boiling heat transfer.

Following the decision to not make new microstructured surfaces this year and the discovery of contamination in the experimental fixture, a new experimental procedure materialized. Plain surfaces were observed to take on a widely-varied wettability upon contamination by particles in the fixture, and this property was exploited in order to compare the bubble size at departure to the surface wettability. Bubble departure was studied by capturing

images of bubbles in flow boiling and comparing the size at departure to the local surface contact angles and fluid flow speed.

2. BACKGROUND

Flow boiling is heat transfer from a surface to a moving liquid which causes it to change to vapor phase. As the fluid progresses either through a channel or across a hot structure, the fluid increases in quality (defined as the vapor mass to total mass ratio) and the fluid and thermal interactions go through many stages. For the many applications of flow boiling, increasing the boiling heat flux for a given wall temperature is often useful. By examining the parameters that govern the heat flux, which in all but the latest stages of flow boiling occurs through the generation of bubbles, it may be possible to design surfaces and geometries that improve the performance of systems that use boiling.

Boiling is an excellent form of heat transfer because of the very high heat fluxes that can be achieved with normal materials and relatively small temperature differences. In any kind of boiling—pool boiling, in which the water is stagnant on the heater, or flow boiling, in which convection with the heater is forced—heat conducts through the water near the surface and locally heats it to above the saturation temperature. At a suitable nucleation site, that superheated water evaporates, becomes a growing bubble. When the bubble departs from the surface, it disrupts the water around it, allowing cold water to come near the surface where it heats up. By constantly moving the water, the bubbles in boiling allow the conduction distance through the water to be very short, greatly lowering the thermal resistance (compared, for example, to conduction or natural convection without boiling) and increasing the heat transfer coefficient. However, the bubbles themselves are made of very low-conductivity vapor and any area of the surface that is covered at a given time by bubbles is a region that is not releasing much heat. Therefore, understanding the interactions between bubbles and the surface in boiling is key to improving heat fluxes in boiling.

In pool boiling, much research is in progress on increasing the critical heat flux (CHF). CHF occurs in pool boiling when the rate of bubble nucleation increases so much that film boiling begins. In film boiling, the bubbles form a film of gas through which the dominant mode of heat transfer is generally radiation. The thermal resistance of the gas film is greater than that of conduction through water in nucleate boiling, so the heat flux out of a hot object (such as a microprocessor) begins to decrease if the heat generation is unchanged. This causes the temperature to rapidly increase until the radiant heat flux eventually surpasses the CHF, at which

point the surface is so hot that most metal parts will have melted. Theoretical correlations that predict the CHF, such as Equation 1, generally predict it independently of surface conditions:

$$\dot{q}_{crit} = Kh_{fg} \left[\sigma g \rho_g^2 (\rho_f - \rho_g) \right]^{\frac{1}{4}}, \quad (1)$$

where \dot{q}_{crit} is the CHF, K is a geometric constant, σ is fluid surface tension, g is gravitational acceleration, and ρ_f and ρ_g are densities of the liquid and gas, respectively [3]. However, recent research has shown that hydrophilic microstructured surfaces can substantially increase the CHF [2]. Using microfabrication to create very hydrophilic surfaces that encourage bubbles to depart earlier, leaving a greater contact area between the hot surface and the water, can achieve an increase in the CHF [2].

CHF applies to pool boiling only, but the coalescence of bubbles into a film is likely to impair heat transfer in flow boiling as well. Flow boiling is more complicated, with the boiling type and heat flux varying with, wall temperature fluid velocity, and quality. Figure 2.1 shows the regions of flow and heat transfer behavior in flow boiling in vertical tubes.

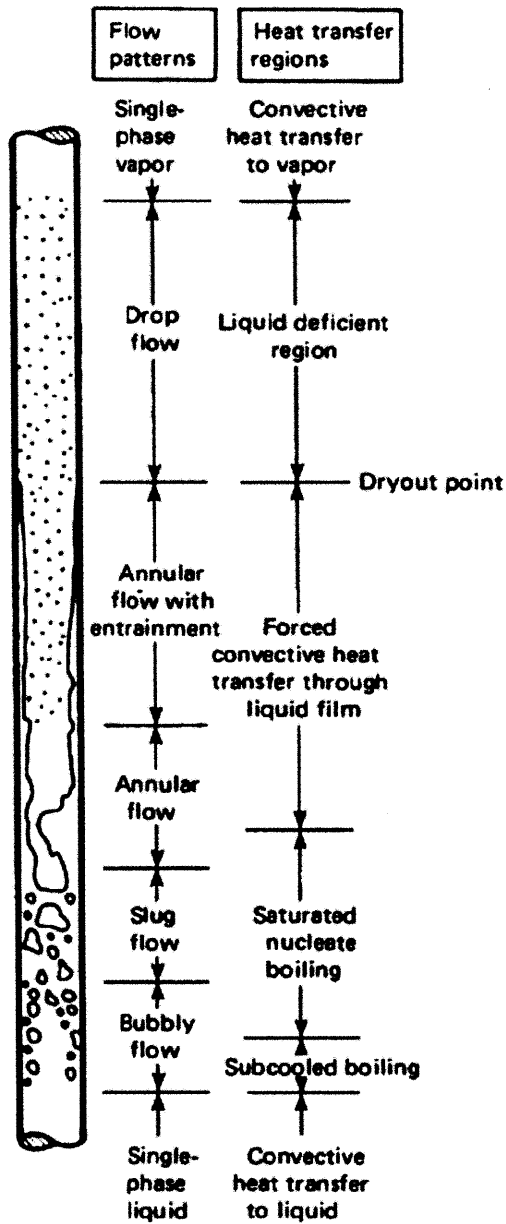


Figure 2.1. Regions of film boiling in a vertical tube with flow from bottom to top. Image adapted with permission from *A Heat Transfer Textbook* by J. H. Lienhard IV and J. H. Lienhard V [4].

Flow boiling looks different depending on the steam quality, wall temperature, and boiling geometry. For instance, flow boiling in a horizontal tube or channel, such as the one used in this experiment, will exhibit different multi-phase flow behavior than what is shown in Figure

2.1, above. However, in any geometry, the earliest (lowest-quality, and therefore occurring at the beginning of the heated region) regions of flow boiling involve individual, quasi-spherical bubbles. As shown in Figure 2.1, this region is called bubbly flow. The first part of bubbly flow is classified as subcooled boiling because some of the fluid has not yet risen to saturation temperature, but boiling can still occur because the water near the heater surface is above saturation temperature. The boiling analyzed in this work is subcooled boiling at a low heat flux, where the fluid bulk temperature has not reached saturation temperature and bubbles are sparse.

An important characteristic of a surface in boiling is its wettability by the fluid, which is quantified by the contact angle between the fluid and the surface in the presence of the fluid's vapor. The contact angle is the angle formed by the surface and the plane tangent to the surface of the fluid at the intersection with the surface. Around a bubble, the contact angle is again (in this work) taken to be the contact angle of the fluid with the surface. When the fluid is water and the contact angle is less than 90° , leading to flat droplets and round bubbles, the surface is considered to be hydrophilic. When the contact angle is more than 90° , round droplets and flat bubbles form, and the surface is considered hydrophobic. Figure 2.2 illustrates the contact angle for a droplet and a bubble.

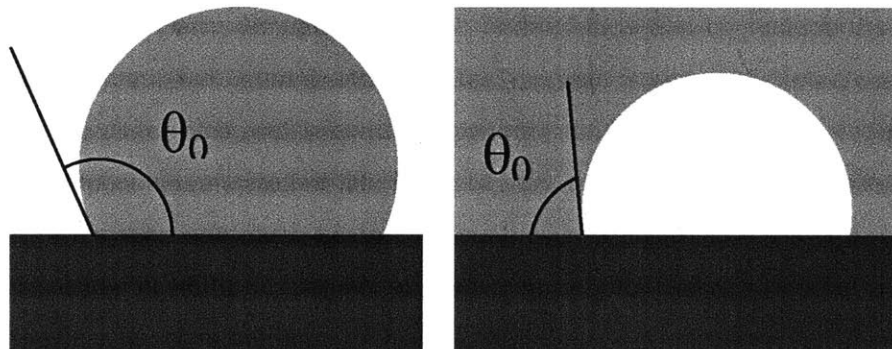


Figure 2.2. Contact angle for liquid-vapor-solid interfaces: a droplet on a hydrophobic surface (left) and a bubble on a hydrophilic surface (right).

Drops and bubbles form the shapes they do because each interface has surface energy. The equilibrium contact angle is reached when the total surface energy of the liquid-gas-solid system is minimized on a surface normal to the direction of gravity. Young's equation gives the equilibrium contact angle, θ_0 , as a function of the surface energies of the three interfaces:

$$\gamma_{SV} - \gamma_{SL} = \gamma \cos \theta_0, \quad (2)$$

where γ_{SL} and γ_{SV} are the surface energies of the solid-vapor and solid-liquid interfaces, respectively, and γ is the surface tension (or surface energy) of the liquid interfacing with its own vapor [5].

For a droplet on a tilted surface, the contact angle is not constant around the contact line. As the tilt is increased, the maximum angle around the droplet increases and the minimum decreases. The maximum angle when the droplet begins to slide is called the advancing contact angle and the minimum is called the receding contact angle. When the equilibrium contact angle is not known, it can be approximated to be a weighted average of the advancing and receding contact angles, θ_R and θ_A , respectively, as given by Equations 3 through 5 [5].

$$\theta_0 = \arccos \left(\frac{\Gamma_A \cos \theta_A + \Gamma_R \cos \theta_R}{\Gamma_A + \Gamma_R} \right), \text{ where} \quad (3)$$

$$\Gamma_R = \left(\frac{\sin^3 \theta_R}{2 - 3 \cos \theta_R + \cos^3 \theta_R} \right)^{1/3} \text{ and} \quad (4)$$

$$\Gamma_A = \left(\frac{\sin^3 \theta_A}{2 - 3 \cos \theta_A + \cos^3 \theta_A} \right)^{1/3}. \quad (5)$$

The equilibrium contact angle is a weighted average because of the cosine in Equation 2 and the nonlinear (to state the obvious) dependence of $\cos \theta$ on θ .

Knowing the contact angles allows for the estimation of the balance of forces that prevents a bubble from departing. S.G. Kandlikar found expressions for the forces on a bubble that lead to departure in subcooled flow boiling based on forces due to surface tension, buoyancy, drag, pressure difference, and momentum changes [6]. These expressions assume a truncated-spherical bubble geometry for the momentum and drag calculations and a two-part geometry for the surface tension, buoyancy and pressure difference calculations. They also assume low flow velocity and a constant wettability surface. For this paper, a simpler model will be developed using the contact angles and bubble height measured and only considering the surface tension and momentum change forces. Kandlikar also does not assume the bubble is a rigid body, which the model here will. Kandlikar makes the important distinction that the advancing and receding contact angle of a droplet on a surface are not equivalent to the upstream and downstream contact angles of the water around a bubble in a flow because the advancing and

receding are the maximum and minimum contact angles and the upstream and downstream angles lie between those values [6]. In this paper, the local equilibrium contact angle of the surface will be estimated to be the average of the upstream and downstream contact angles as measured at the moment before departure.

This work will estimate the bubble dimensions at departure based on a rigid-body force balance in the direction of fluid flow. The flow-direction force balance is assumed to dictate the departure rather than the forces normal to the surface. Only two forces will be considered: the force in the direction of the flow (the x-direction) due to the change in momentum of the water behind the bubble and the force in the negative-x-direction due to the x-component of the surface tension around the bubble. Shear forces and the force due to the pressure drop in front of the bubble are neglected in this analysis. Viscosity-driven pressure drop along the length of the channel is also neglected.

The force of the water behind the bubble will be found via conservation of momentum, assuming that the x-direction momentum goes to zero for the fluid over the area of the bubble as projected in the plane perpendicular to x. For this calculation, the bubble is assumed to take the shape of a sheared truncated sphere, which has a truncated circle for a flow-direction cross-section and a circle for a contact area. The heated region of the channel is not beyond the fluid entry length so a parabolic laminar flow profile cannot be assumed, and the presence of other bubbles in the channel makes the velocity profile almost impossible to predict. For simplicity, the fluid velocity is assumed to be in the x-direction only and the profile is assumed to be constant throughout the channel, except when encountering the bubble in question. Steady-state conservation of momentum states that the net force in the x-direction, F_x , on a control volume is related to the net momentum flux out of the control volume, as given in Equation 6. ρ is the water density, \vec{v} is the water velocity, and v_x is the x-component of velocity, where $v_{x,in}$ and $v_{x,out}$ denote the velocity entering and exiting the control volume, respectively. Based on the assumptions given above, $v_{x,in}$ is equal to the bulk water velocity, v , and $v_{x,out}$ is zero. Therefore,

$$\sum F_x = \int \rho v_x (\vec{v} \cdot \hat{n}) dA = \rho A (v_{x,out}^2 - v_{x,in}^2) A = -\rho v^2 A \quad (6)$$

The net force in the x-direction on the water behind the bubble is found to be $-\rho v^2 A$, which is equal and opposite to the force exerted on the bubble by the water, $\rho v^2 A$. This force should take the form of a pressure difference between the water behind and in front of the bubble, but only the magnitude is relevant for this analysis.

The surface tension force is assumed to be equal to that of a bubble with a square base of side length equal to the diameter of the circle where the bubble contacts the surface. The edges of the square that are parallel to the flow will not contribute to the x-component of the force, and the upstream and downstream edges are assumed to contact the surface at the upstream and downstream contact angles, respectively. These x-direction surface tension forces are equivalent to those on a bubble with a circular base where the front half of the bubble contacts the surface at the downstream contact angle, θ_d , and the back half at the upstream contact angle, θ_u .¹ The surface tension forces, along with the force of the water behind the bubble, are shown graphically in Figure 2.3.

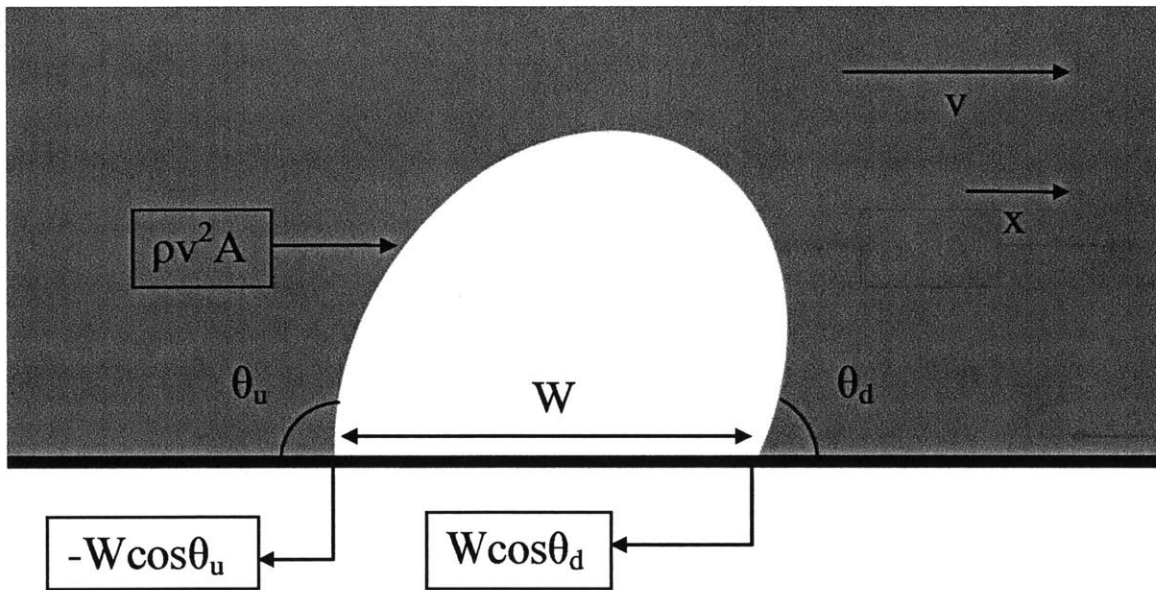


Figure 2.3. The flow-direction force balance on a bubble in a left-to-right flow. Forces are given in the direction of arrows, not necessarily in the x-direction. The subscripts u and d denote upstream and downstream, respectively.

The length in the direction of flow that the bubble contacts the surface will be called the width, denoted as W in Figure 2.3 and in the following equations. The force balance illustrated in Figure 2.3 leads to the following equation:

¹ A simple integration around the circular contact line will show that this is true.

$$\rho v^2 A = \sigma W (\cos \theta_d - \cos \theta_u), \quad (7)$$

where A is the projected area perpendicular to the direction of the flow. This force balance will be true at all times, not just at the moment before departure. Departure will occur at a critical moment where one term changes and the other cannot, such as when one or both of the contact angles reach the advancing or receding contact angles of the fluid-vapor-surface combination.

The shape projected in the x-direction is assumed to be a truncated circle with contact angles θ_a equal to the average of the upstream and downstream contact angles. For angles in radians, the area and radius, r , are given by Equation 8 and 9.

$$A = \pi r^2 \left(1 - \frac{\theta_a}{\pi}\right) + r^2 \cos \theta_a \sin \theta_a, \text{ where} \quad (8)$$

$$r = \frac{W}{2 \sin \theta_a}. \quad (9)$$

Substitution of Equations 8 and 9 into Equation 7 results in a force balance as a function of W :

$$\frac{\rho v^2 W^2}{4 \sin^2 \theta_a} (\pi - \theta_a + \cos \theta_a \sin \theta_a) = \sigma W (\cos \theta_d - \cos \theta_u). \quad (10)$$

Solving for W leads to the following equation for bubble width at departure as a function of the upstream and downstream contact angles:

$$W = \frac{4\sigma (\cos \theta_d - \cos \theta_u)}{\rho v^2} \cdot \frac{\sin^2 \theta_a}{\pi - \theta_a + \cos \theta_a \sin \theta_a}, \text{ where} \quad (11)$$

$$\theta_a = \frac{\theta_d + \theta_u}{2}. \quad (12)$$

Assuming again that the bubble's x-direction projected area is a truncated circle, the bubble's height, H , can be found from the width and average contact angle with Equation 13:

$$H = W \left(\frac{1 + \cos \theta_a}{2 \sin \theta_a} \right) = \frac{2\sigma (\cos \theta_d - \cos \theta_u)}{\rho v^2} \cdot \frac{\sin \theta_a (1 + \cos \theta_a)}{\pi - \theta_a + \cos \theta_a \sin \theta_a}, \quad (13)$$

where θ_a can be found in Equation 11.

3. METHODS

3.1 Experimental Apparatus

In this experiment, deionized and degassed water is boiled on flat silicon surfaces in forced convective flow. The experimental fixture allows for the collection of video of bubbles in flow boiling. The bubbles are viewed from the side with a microscope to capture the upstream and downstream contact angles. A pump pushes water through a preheater which brings the water to near saturation temperature and a small heater on the back side of the silicon surface initiates boiling, which is captured by the camera. The fluid cools through a heat exchanger, completing the loop. Figure 3.1.1 shows a schematic of the experimental apparatus.

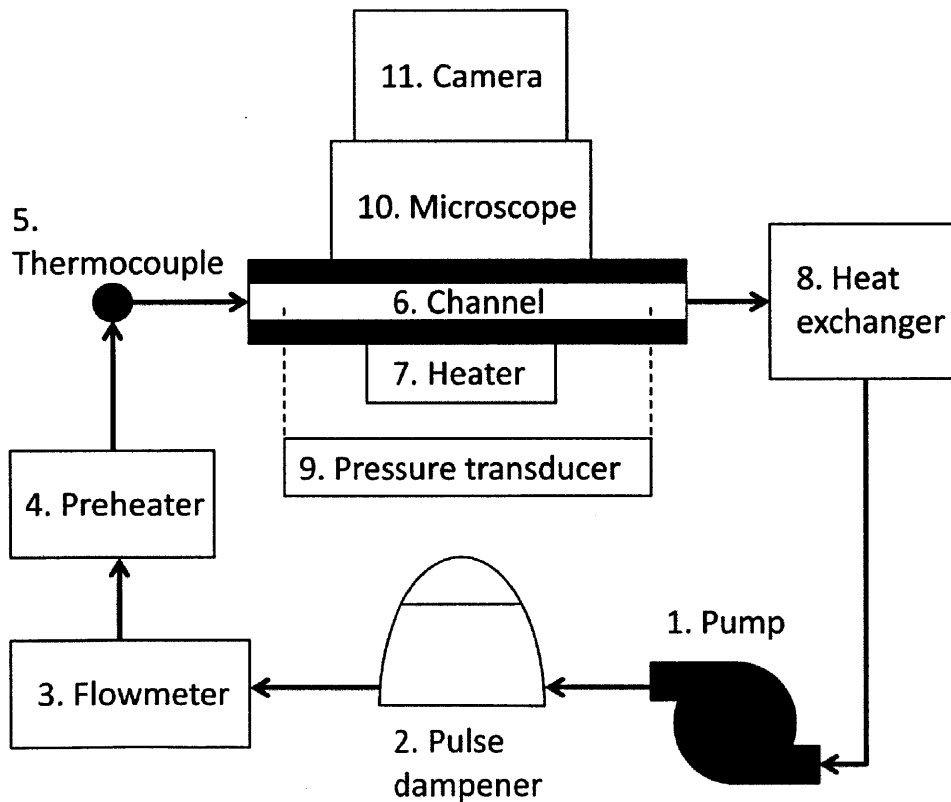


Figure 3.1.1. A schematic of the experimental apparatus. Water flow lines are indicated by bold arrows. The numbered elements are described in detail in the text below.

Figure 3.1.1 shows the setup of the experimental apparatus. Numbered elements are detailed in the following list:

1. Peristaltic pump: Cole-Parmer #7553-70, 6-600 rpm with Masterflex Easy-Load II head #77200-62 and Masterflex size 15 silicone tubing.
2. Pulse dampener: Cole-Parmer #07596-20. Trapped (easily compressible) air absorbs pulses of fluid from peristaltic pump for more even flow through the channel.
3. Flowmeter: Omega FLR 1000-ST.
4. Preheater: copper coiled tube, 1/4" ID, 2.7 m long, heated by 30.5 Ω coiled wire heater controlled by Variac transformer #TDGC-2KM which outputs 0-130 VAC at 60Hz .
5. Thermocouple: Omega thermocouple read by Stanford Research Systems #SR630 16 channel thermocouple monitor.
6. Channel: 0.67 mm x 4.65 mm x 20mm minichannel housed in sample holder. See Figures 3.1.2 and 3.1.3 below for details.
7. Heater: 1 mm x 1 mm gold deposited resistive heater with resistance of 163 Ω controlled by a 25V power supply. Typically 8-10 V was used.
8. Heat exchanger: Lytron #6310G3SB copper tubing with Mechatronix fan #UF25GC12.
9. Differential pressure transducer: Setra #2301005PD2F2DB. Senses 0-5 PSID. Data from this sensor was not collected or used in this experiment, but could be used in future research.
10. Microscope: Nikon Eclipse #TE2000-U at 10x*1.5x magnification with mercury lamp controlled by X-cite Series 120.
11. Camera: Vision Research model Phantom v7.1 with Phantom camera control software.

All elements were connected by tubing of silicone and an unknown plastic using stainless steel and brass compression fittings. Various parts of the fixture were sealed with silicone RTV.

The silicon minichannel is housed in a sample holder made of polycarbonate (PC) with Teflon (PTFE) spacers holding the channel in place. A glass front plate is held on by bolts and sealed by an o-ring. Figure 3.1.2 shows the sample holder.

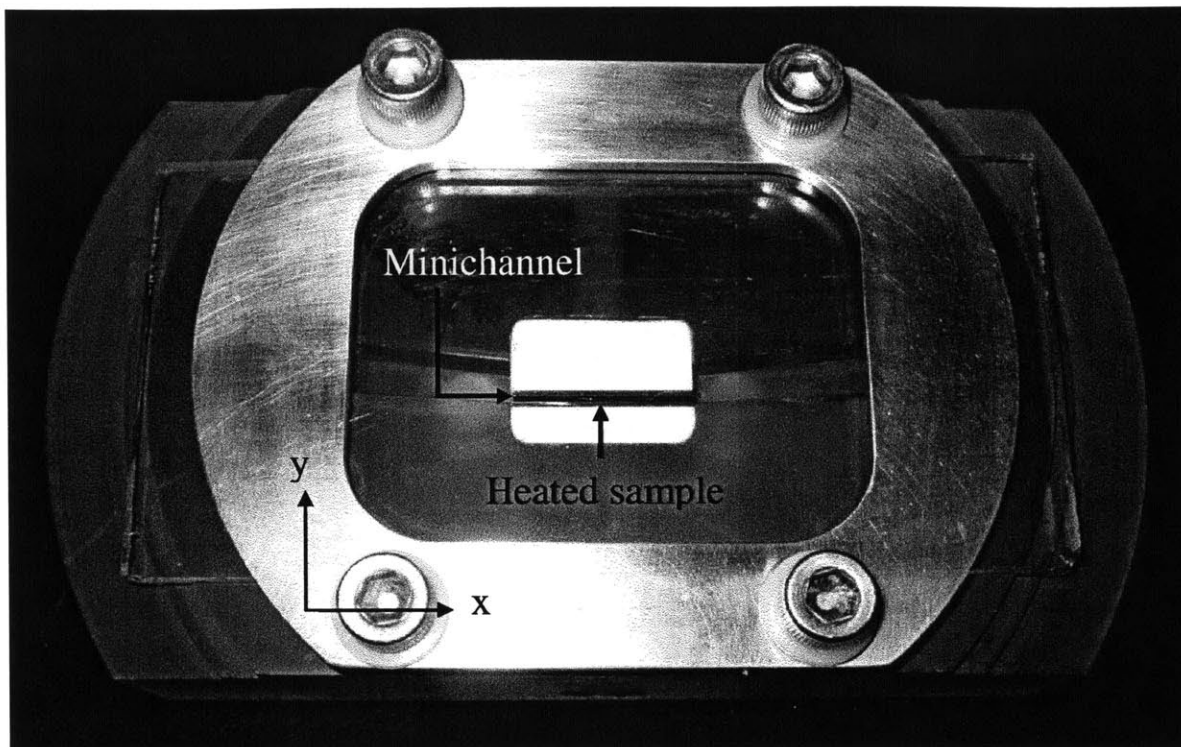


Figure 3.1.2. A photograph of the sample holder with the channel and heated surface indicated by arrows. Water enters and exits from the back. x and y directions are given to clarify Figure 3.1.3, which shows a schematic of the channel.

Figure 3.1.2 shows the sample holder and indicates the channel and the heated sample where boiling occurs. Water enters and exits from the back. The minichannel consists of three squares of silicon sandwiched between two PTFE blocks. The glass plate forms the front wall. A schematic of the channel is shown in Figure 3.1.3 below.

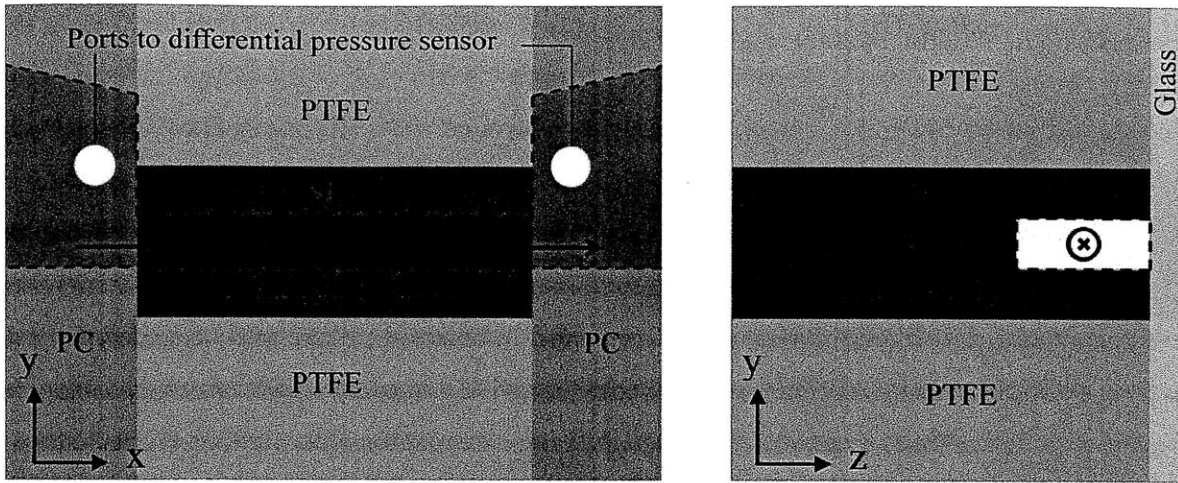


Figure 3.1.3. The channel is shown schematically from the front (at left) and from the side, looking through the channel (at right). The channel is outlined with a dashed line and arrows indicate the direction of flow. The bottom silicon piece contains the heater and the surface of interest. The transition from the PC channel to the silicon minichannel is abrupt. The eddies that are likely to form there may obscure the pressure readings, which were not collected for this analysis. The right-handed x , y and z coordinates relate this schematic to the photograph in Figure 3.1.2.

As shown in Figure 3.1.3, the channel is a silicon sandwich in which the bottom piece contains the heater and the surface of interest. Water flows from the larger PC channel to the thinner and shallower silicon channel. The transition from the PC channel to the silicon channel is abrupt. The eddies that are likely to in the transition region may obscure the pressure readings, which were not collected for this analysis. However, this may cause problems in future research using this same fixture.

The sample itself has two sides, on one a smooth and (initially) clean silicon surface and on the other a deposited gold resistive heater. Figure 3.1.4 shows the heater on the back side of the surface.

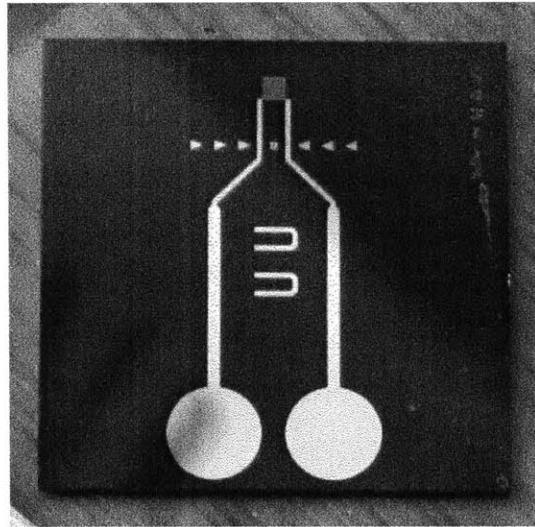


Figure 3.1.4. The thin film gold heater on the back of the surface. The pale square at the top of the gold pattern is the heating element, which has a resistance of 163 Ω .

The heater itself is 1mm x 1mm and has a resistance of 163 Ω . The round gold pads allow spring-loaded electrodes to apply power from the 25V (max) power supply. The sample and other silicon pieces are cut from a 15 cm diameter, 0.675 mm thick silicon wafer.

Before data collection, the fixture is cleaned with deionized water. The sample and other silicon parts are cleaned with methanol, isopropyl alcohol, and deionized water (in that order) and dried under a nitrogen gas flow. Then the sample is plasma cleaned in oxygen for 15 minutes and installed in the fixture.

3.2 Video Collection

In this experiment, information is gained by analyzing video of the bubble nucleation, growth and departure as a function of surface wettability and water flow rate. After the surface is prepared and installed, the system is filled with degassed water and closed. For each of three flow rates, video of the bubbles in the channel is recorded while the system is in steady state.

First, the prepared sample and other parts are inserted into the clean sample holder. The heater electrodes are screwed in and electrical continuity is confirmed. The glass, which has been plasma cleaned with oxygen for 15 minutes to improve wettability, is placed over the open channel under a slow flow of DI water to minimize the amount of air trapped under the glass.

The glass is attached with screws and the sample holder is attached to the rest of the fixture with compression fittings.

Water is boiled on a hot plate in 1L Erlenmeyer flasks to remove dissolved gas. The water is cooled in air to 55C to prevent damage to the flowmeter. This water is then introduced into the system just upstream of the pump to flush the existing water, which may contain dissolved gas, out. Some air is allowed to remain in the pulse dampener to absorb the pulses of fluid that come from the pump. When the system is filled with degassed water, it is closed by connecting the outlet and inlet via compression fittings under a bowl of degassed water. In practice, not all air is removed from the system, but this method seems to minimize it.

The pump, preheater and heat exchanger fan are turned on and the water temperature begins to rise. The preheater voltage is controlled manually using optical feedback from the microscope until the water exiting the preheater reaches steady state at the highest possible temperature that does not cause bubbles of dissolved air to nucleate in the microchannel. The pressure in the channel is approximately atmospheric but the exact pressure is not known. The surface heater is turned on at 6V and then the voltage is raised until a reasonable rate of nucleation is reached in the center of the channel, around 8-10V. The fixture position is adjusted to record the farthest- upstream nucleation sites, rather than those closest to the heater, in order to avoid premature departure due to jostling from bubbles that have already departed upstream. The microscope is focused on the bubbles and then switched to the camera, which has been turned on. The mercury lamp is turned on, the reflective light turned off, and the microscope refocused for the camera based on the preview on the computer screen. The lamp brightness, microscope aperture and camera exposure are adjusted to obtain the best picture of the nucleating bubbles, especially of their contact points with the surface.

Bubble video is recorded at three flow rates for each surface. The minimum is the smallest flow rate that produces reasonably steady flow and small enough bubbles that clear video can be recorded. The maximum would be the greatest flow rate that could be heated by the preheater to a temperature where bubbles will nucleate in the channel, but in practice it is the largest flow rate that can be heated without making the preheater insulation give off fumes.

When the system is running in steady state and the video preview is clear, video is recorded at 30 frames per second at a resolution of 600x800 pixels. Greater resolution in time was not possible due to the very long time to compile the large videos collected. While video is

being collected, the flow rate is observed in LabVEIW and the channel inlet temperature is recorded. Video collection is stopped after six minutes (the largest possible duration allowed by the camera for the given resolution and frame rate) and the fixture is brought to equilibrium for the next test flow rate while the video compiles.

After recording videos at all flow rates, the entire fixture except the pump and fan are turned off. After the preheater has cooled enough to prevent pool boiling, the pump and fan are shut off.

3.3 Experimental Parameters

Video was collected for two surfaces: one that was clearly contaminated from use in evaluation of the fixture performance and for a short time in air and one that was oxygen plasma cleaned the day of the video collection. The freshly-cleaned one quickly became contaminated during flow boiling testing. Because the second surface became contaminated and because the video quality was inferior, no data analysis was performed from the video of boiling on the second surface. Only the video of the first contaminated surface was used for data analysis.

Video was collected of the contaminated surface in flow boiling with the experimental parameters given in Table 1.

TABLE 3.3.1. Experimental parameters for evaluation of flow boiling on the contaminated surface.

Flowmeter Voltage (V) Flow rate (mL/min)	Inlet Temp. (C)	Preheater Voltage (V)	Surface Heater Voltage (V)	Flow Speed (m/s)
70	90.6	95	8	0.37
135	87.5	112	8	0.72
197	80.2	124	8	1.05

Flow speed was calculated from the flowmeter voltage and channel dimensions. Inlet temperature was determined such that the frequency of bubble departure in the channel was moderate. The inlet temperature is significantly lower than the saturation temperature of water at atmospheric pressure because of the presence of dissolved air in the water despite attempts to remove it. Thus, the bubbles that form are likely to contain a mixture of air and steam, but the forces that govern the bubbles and their shape and size at departure should be very nearly equivalent to those which govern bubbles of steam in boiling.

3.4 Data Extraction

Bubble size and contact angle were found for bubbles in the moment before departure from the surface with a MATLAB script involving clicking at predetermined places in stills extracted from the boiling videos.

Video was reviewed to find bubbles at the moment before departure. Changes in the surrounding bubbles were observed to determine whether the bubble departure was due to the forces exerted on it by the flow and the surface or due to a collision or coalescence with another bubble. An example of a bubble that clearly did not depart of its own accord is given in Figure 3.4.1.



Figure 3.4.1. An example of a series of video frames which indicate that the departure of a bubble was premature and thus should not be used in data analysis. In this case the bubble appears to have been pushed off by another bubble, as indicated by the shadow in the central image.

The shadow in the middle image of Figure 3.4.1 is probably that of some larger bubbles which were generated in the preheater and entered the channel. Shadows like this were a clear indication that any bubbles departing at that time should not be analyzed. The bubbles around the departing bubble were also examined to determine the reason for departure. If bubbles upstream of the bubble in question or bubbles on the opposite side of the channel also departed or changed shape or size at the same time, none of the bubbles departing at that time were considered. Pictures were extracted just before the departure of bubbles that departed on their own. Pictures were also taken of other interesting bubble phenomena.

For departing bubbles, a MATLAB script was written to find the bubble width (the length, in the direction of flow, of the contact area of the bubble with the surface) and downstream and upstream contact angles. Points of interest were clicked on with position information recorded by the built-in function *ginput*. The sequence of clicks, shown in Figure 3.4.2, was repeated three times and averaged to reduce human error.

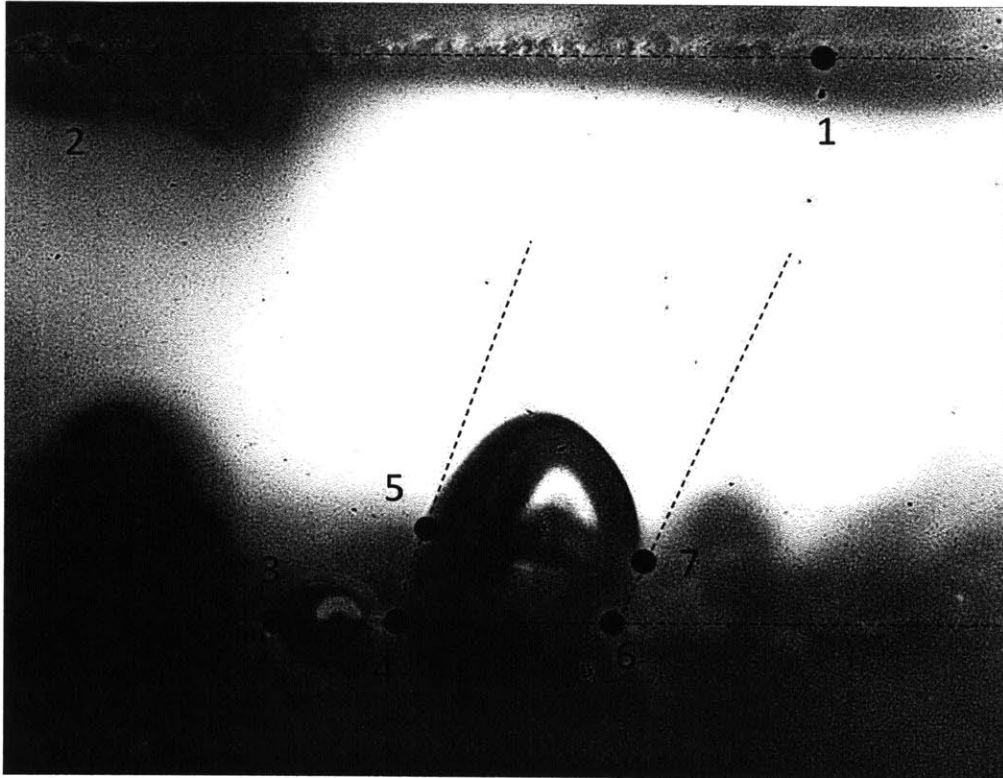


Figure 3.4.2. The inputs into the MATLAB script for calculation of channel height, bubble width, and downstream and upstream contact angles. Point 3 was placed at whichever point on the top surface was clearest.

The 21 clicks that made up three full cycles of seven spatial inputs were averaged to get the seven points shown in Figure 3.4.2. Bubble width and contact angles, as well as the channel width in pixels, were calculated by the script based on the averaged inputs. The channel width in pixels was compared to the known channel width of 0.67 mm to find the sizes in mm of other bubble dimensions.

A separate but similar function was used to find the bubble height—the maximum dimension perpendicular to the surface—for a picture with a known mm-to-pixel ratio. The sequence of clicks used to find the height is shown in Figure 3.4.3. As before, three cycles of inputs were averaged before being used to find the height.

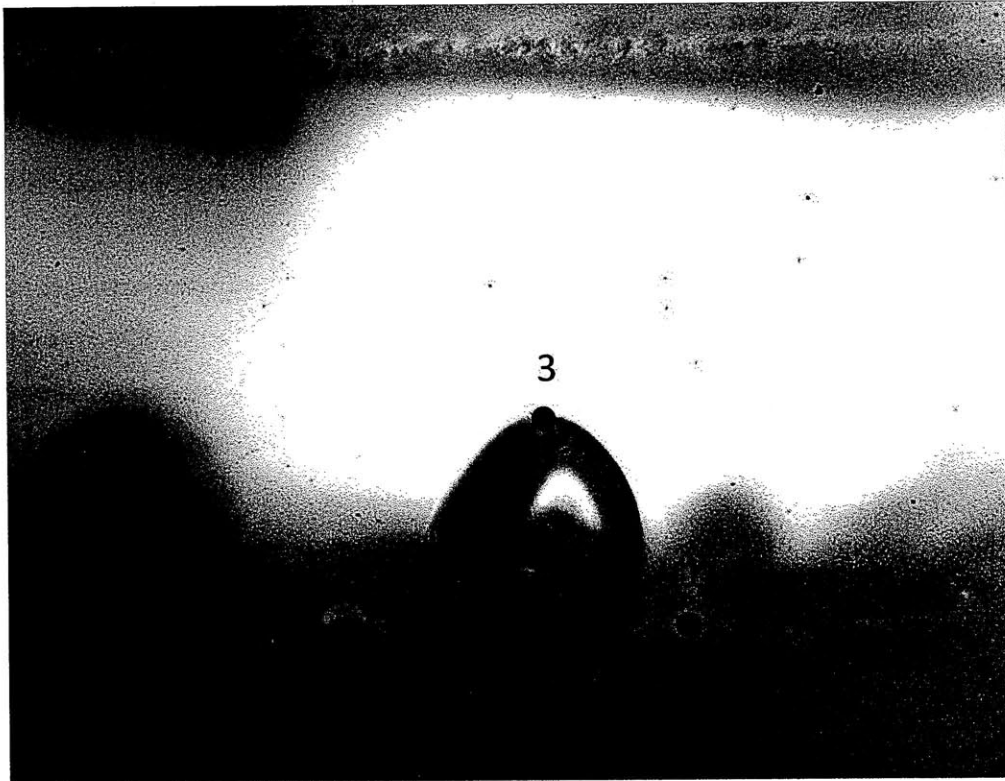


Figure 3.4.3. The inputs into the MATLAB script for calculation of bubble height for an image with known channel height.

The second script is separate because the decision to measure bubble height came later. If this experiment were to be repeated, it would be beneficial to combine the two scripts. Both scripts are included in Appendix II.

Bubble height, width, and downstream and upstream contact angles are poor measures compared to volume and contact area, which cannot be found because the bubble dimensions perpendicular to the plane of the video are unknown. The dimensions that were measured will, however lend some insight. Further study will have to determine the effects of bubble width, height, and contact angle at departure on heat fluxes in flow boiling.

4. RESULTS AND DISCUSSION

4.1 Bubble Departure

Bubble dimensions at departure were collected from video images and compared to the measured contact angles and theoretical predictions for bubble size. A great variety of bubbles were observed, and in all relationships there is a fair amount of scatter. The experimental data shows that bubble width—that is, the length of surface in the direction of flow that is touched by the bubble—increases with equilibrium contact angle and decreases with flow speed. Bubble height (in the direction perpendicular to the surface) is found to decrease with flow speed but show little relationship to contact angle. Theoretical results are shown to have moderate agreement with experimental results, indicating that both width and height decrease with flow speed and increase with equilibrium contact angle and contact angle hysteresis. These results will be detailed in this section.

Stills taken from the flow boiling video give downstream and upstream contact angles and bubble width and height at the moment before departure. Since the video frame rate was 30 frames per second, the bubble size may have been recorded up to 33.3 ms before the actual departure, but because low heat fluxes were used the bubbles grew slowly (over seconds to tens of seconds) and the size difference between the final picture before departure and the actual moment before departure should be minimal. The surface tested was contaminated such that the wettability was not constant, so by comparing the size of the bubble to the local wettability, as estimated by the average of the downstream and upstream contact angles.

The video quality was variable, but the view of the growing and departing bubbles was clear most of the time. Many factors, which will be discussed in detail later, stood in the way of getting clear numerical data from the departing bubbles. Of the 30 minutes of boiling video collected, 25 departing bubbles at three flow rates were clear enough to use in this analysis. Figure 4.1.1 shows one departing bubble.

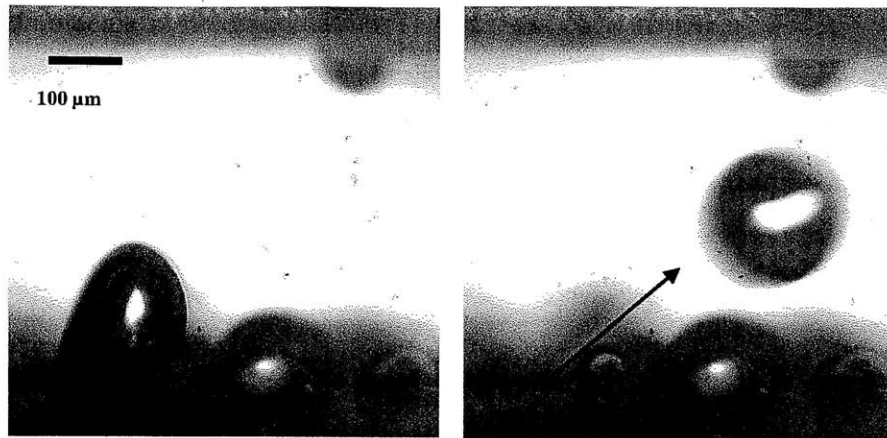


Figure 4.1.1. A bubble before (left) and after (right) departure from the surface.

Several types of bubbles formed on the contaminated surface. Figure 4.1.2 shows four bubble types that were observed with a variety of sizes and contact angles.

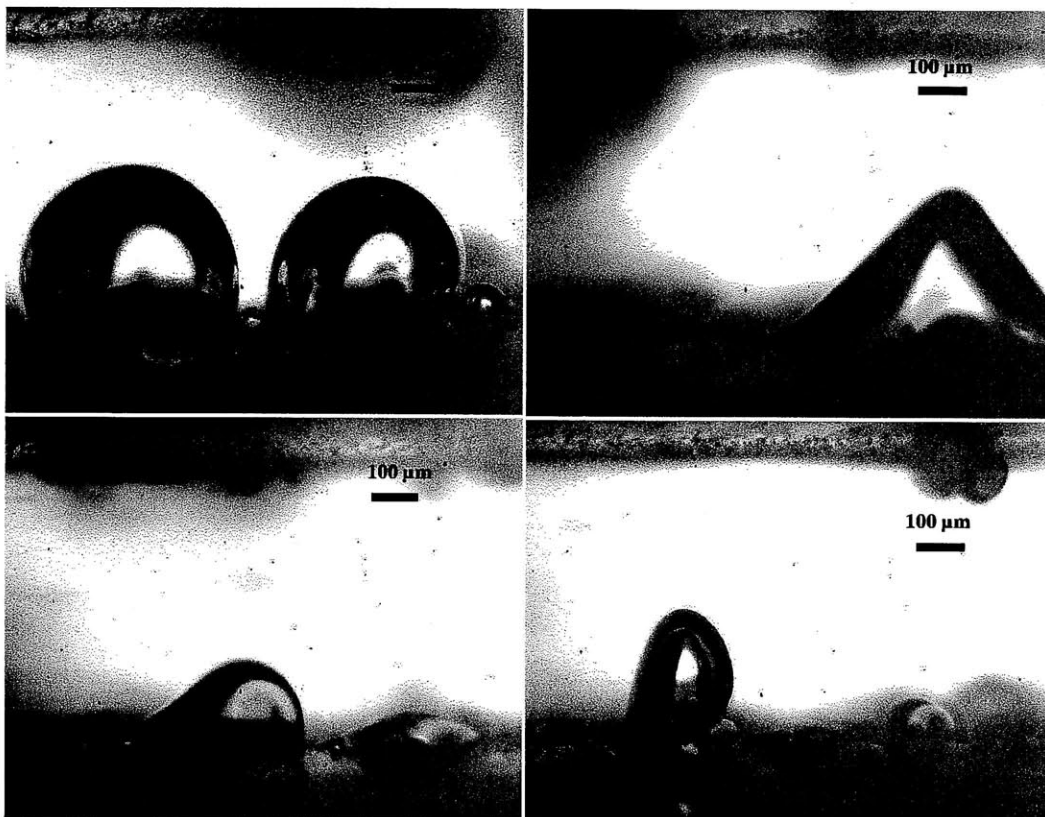


Figure 4.1.2. Bubbles were observed in a variety of sizes and shapes at the moment before departure. The bottom surface is heated and the flow direction is to the right.

Figure 4.1.2 depicts four types of bubble shapes that were observed. Additionally, Appendix I shows images of all departing bubbles. With so many bubble shapes, the relationship between downstream and upstream contact angle in the bubbles observed is weak, as shown in Figure 4.1.3.

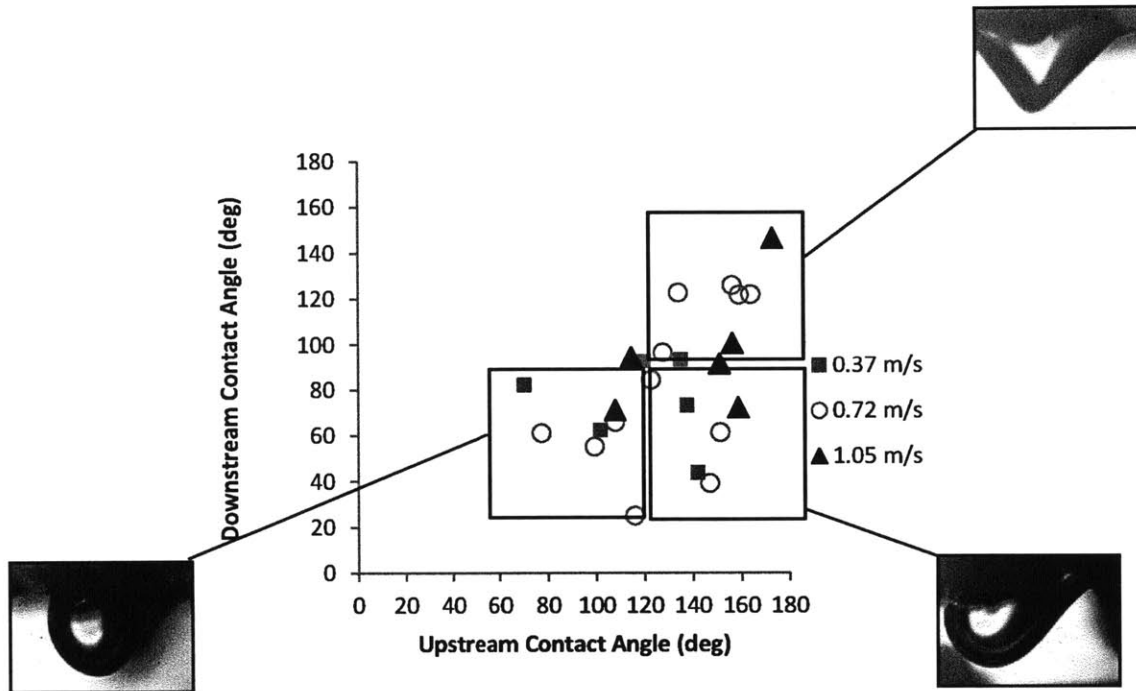


Figure 4.1.3. Downstream (water) contact angle is plotted against upstream contact angle, with bubbles shown representing the three main regions of the plot.

As would be expected for a surface with relatively constant wettability within the region of a bubble, the downstream angle generally increases with increasing upstream angle. However, there is a great spread. The downstream contact angle is generally smaller than the upstream contact angle, consistent with expectations for bubbles in a flow. The contact angles vary for a given flow rate, indicating that the surface has non-uniform wettability. The amount of contact angle hysteresis also varies for a given flow rate, indicating that the wettability variation occurs on a small enough length scale that a single bubble can span multiple zones of wettability. There is also no clear trend in the amount of contact angle hysteresis between the three flow rates, as shown in Figure 4.1.4, which follows.

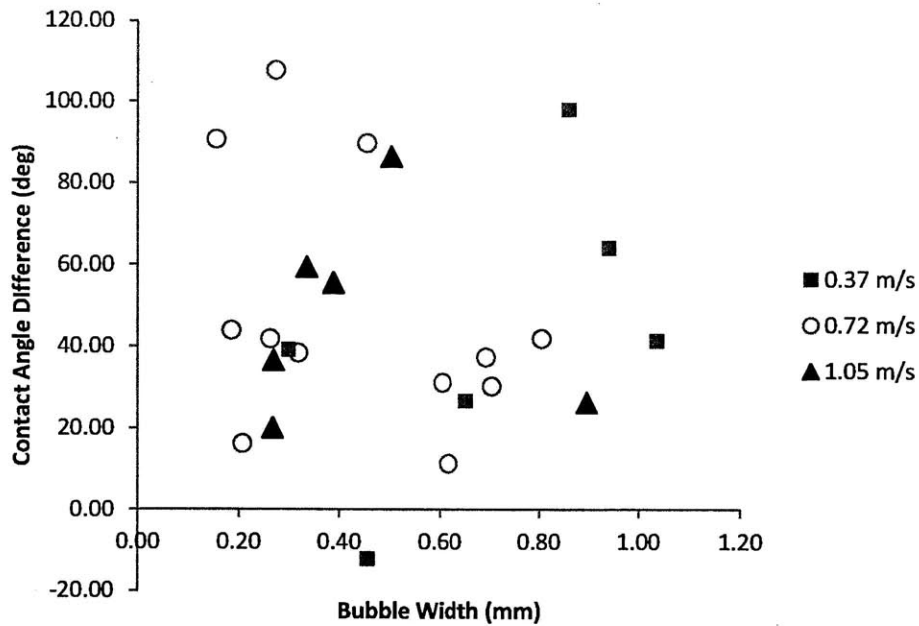


Figure 4.1.4. The contact angle difference is plotted against width for the three flow rates, showing no trend in either set of variables and indicating that the variation in contact angle due to the surface wettability non-uniformity is greater than the variation in contact angles due to the different flow rates used.

The average difference between the upstream and downstream contact angles was 48.9 degrees with a standard deviation of 30.9 degrees.

The contact angle of a still droplet on the contaminated surface was measured using a goniometer. Figure 4.1.5 shows a small water drop on the contaminated surface that was used in the contact angle measurements.

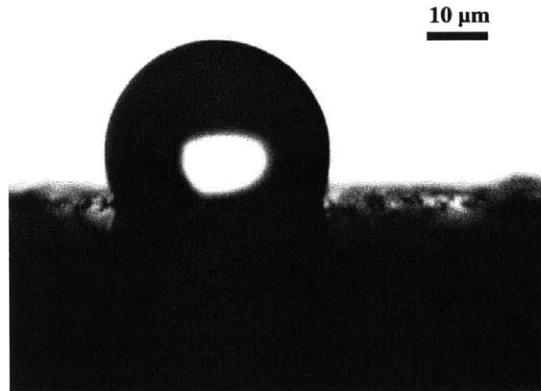


Figure 4.1.5. A water droplet on the contaminated silicon surface during contact angle measurement. The average maximum contact angle at the location tested was 145.3°.

Contamination made the silicon surface hydrophobic, as demonstrated by the obtuse contact angle in Figure 4.1.5, above. The contamination can be clearly seen on the surface. This wafer had originally been cleaned with solvents and then plasma-cleaned with oxygen, but contamination resulted from the use of the wafer in the flow-boiling fixture. A freshly plasma-cleaned silicon surface is shown in Figure 4.1.6.

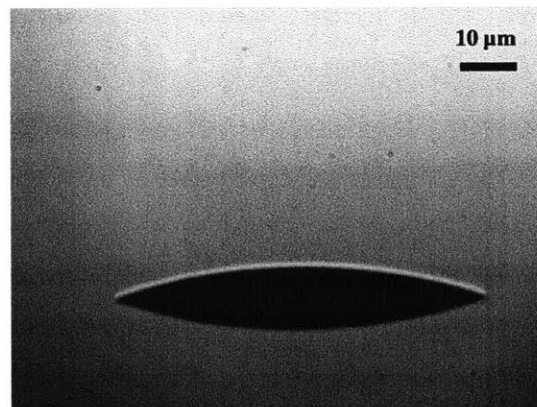


Figure 4.1.6. A water droplet on a smooth, oxygen plasma-cleaned silicon surface during contact angle measurement. The average maximum contact angle was 39.1°.

The low contact angle between the water and the smooth silicon surface shows that the smooth, oxygen plasma-cleaned surface is hydrophilic, in stark comparison to the contaminated surface. The mirror-like finish shows the absence of contamination and surface defects on the surfaces before they are contaminated during use in the fixture.

The contact angle measurements of drops on the contaminated surface, taken shortly after the collection of flow boiling video, are shown in Figure 4.1.7.

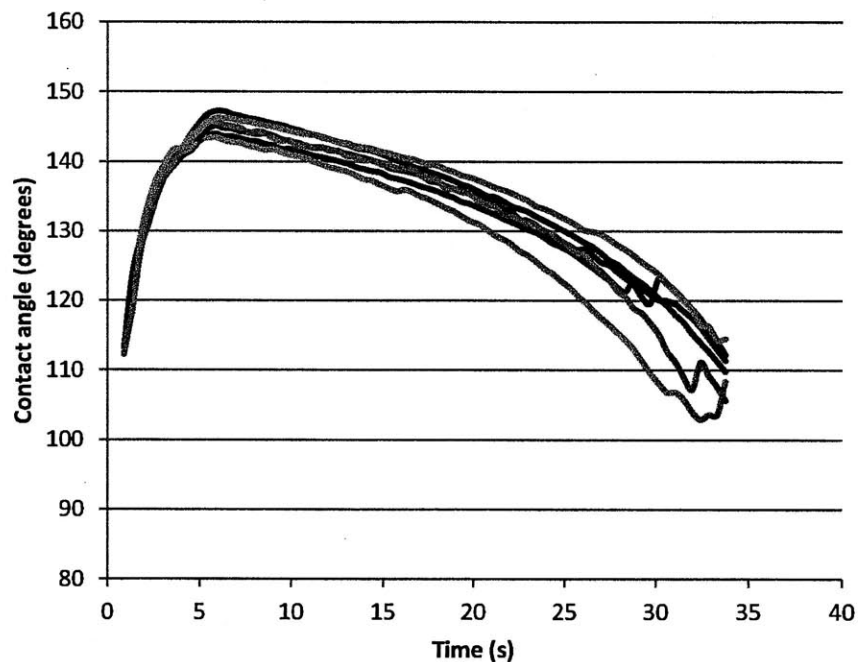


Figure 4.1.7. Contact angle measurements of the contaminated surface, showing an average peak of 145.3°. The six lines represent six series of measurements.

The average maximum contact angle was 145.3 degrees, showing the contaminated surface to be hydrophobic. The standard deviation in maximum contact angle was 1.4 degrees, which is small compared to the distribution in average contact angle seen in the flow boiling video (see Figure 4.1.3). However, the contact angle measurements were all taken at the same location, so only a small variation would be expected. The contact angle of the drop first increases with time while the drop reaches equilibrium and then decreases gradually as the (very small) drop evaporates. The maximum contact angle generally corresponded with the maximum droplet width, when the drop was neither advancing nor receding, and therefore can be assumed

to be the equilibrium contact angle. Because these contact angle measurements were all taken at the same location, the variability in contact angle over the contaminated surface was not demonstrated. On average, the equilibrium contact angle of all bubble departures recorded on the contaminated surface was 106.7° .

Although the original goal of this research was to use several surfaces of different (but constant) wettability, the variable-wettability surface was useful in that it allowed for the examination of bubble departure at many average contact angles on a single surface.

Having examined the wettability of the contaminated surface and found it to be generally hydrophobic but highly variant, the size of the bubbles can be discussed in comparison to the contact angles observed. A variety of bubble sizes and shapes were observed at the moment before departing from the surface. Figure 4.1.8 shows that both the width and the height of the bubbles were highly varied.

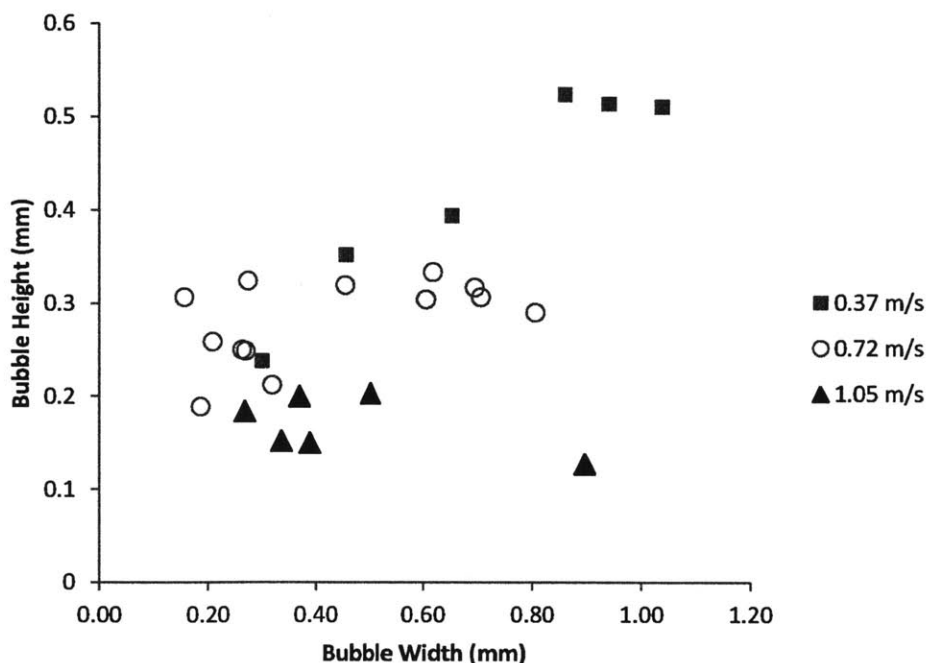


Figure 4.1.8. The width and height of all departing bubbles are plotted, showing the variation in bubble size and the dependence on flow rate of bubble height.

The departing bubbles range from 0.13 to 0.52 mm in height 0.15 to 1.04 mm in width². Figure 4.1.8 shows that for the surface tested, bubble height at departure is inversely related to liquid flow rate regardless of contact angle. The dependence of the bubble width on flow rate is not clear because of the range of contact angles and the strong dependence of bubble width on average contact angle, which is shown in Figure 4.1.9, which follows.

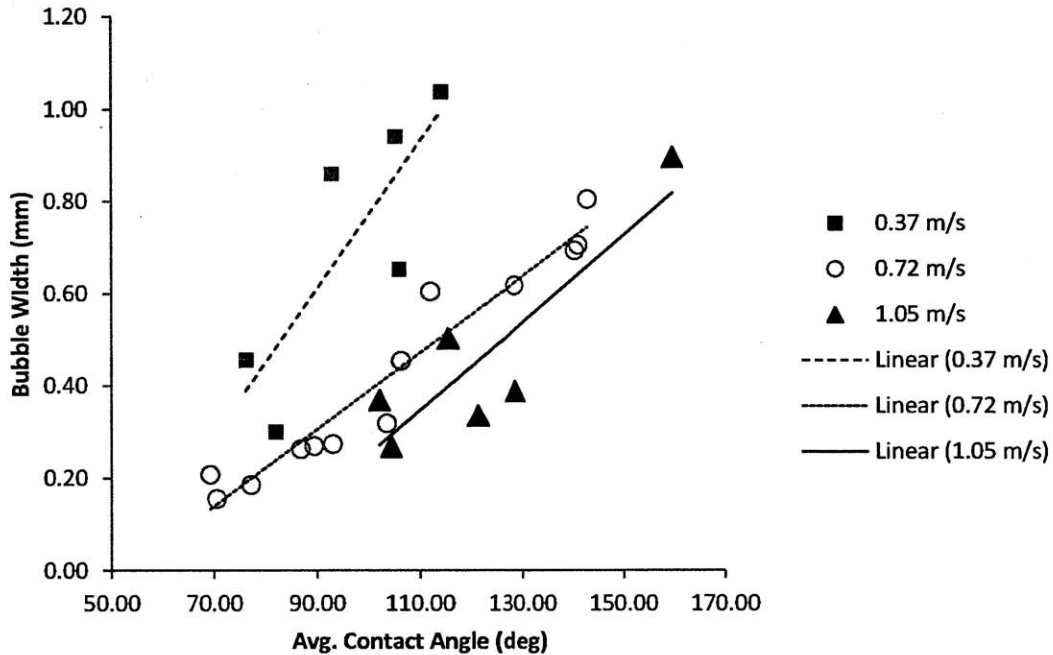


Figure 4.1.9. Bubble width at departure is compared to average contact angle at three water flow rates, given as the bulk velocity of the water in the channel. For each flow rate, the bubble width increases with increasing contact angle. At a given contact angle, lower flow rates produce wider bubbles. Linear fits were applied to the data to show the general trend in bubble width with contact angle, but there is insufficient data to determine if the relationship is linear.

Figure 4.1.9 shows that the bubble width at departure is positively correlated with the average contact angle and inversely correlated with the flow speed. The average (taken over the three flow rates) increase in bubble width is 0.011 mm per degree of water contact angle. This

² For reference, the height of the channel is 0.67 mm.

means that if wider bubbles enhance flow boiling, more hydrophobic surfaces should be employed, and hydrophilic surfaces should be used if narrower bubbles improve boiling.

Bubble width was also compared to the downstream and upstream contact angles to determine if one mattered more, but the results were not enlightening. Figure 4.1.10 shows that although the trend of width vs. contact angle is still generally increasing, the results are more scattered than those with the average contact angle.

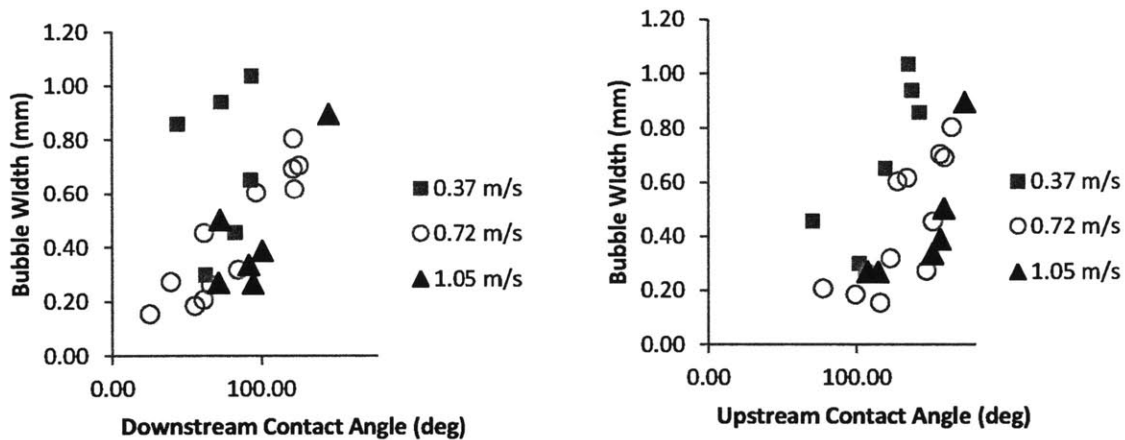


Figure 4.1.10. Bubble width is compared to downstream (at left) and upstream (at right) contact angles, but neither correlation is stronger than that with average contact angle.

Bubble width increases with both downstream and upstream contact angle, though it appears to be more strongly correlated with average (or equilibrium) contact angle.

Bubble height was also measured, and is plotted against average contact angle in Figure 4.1.11.

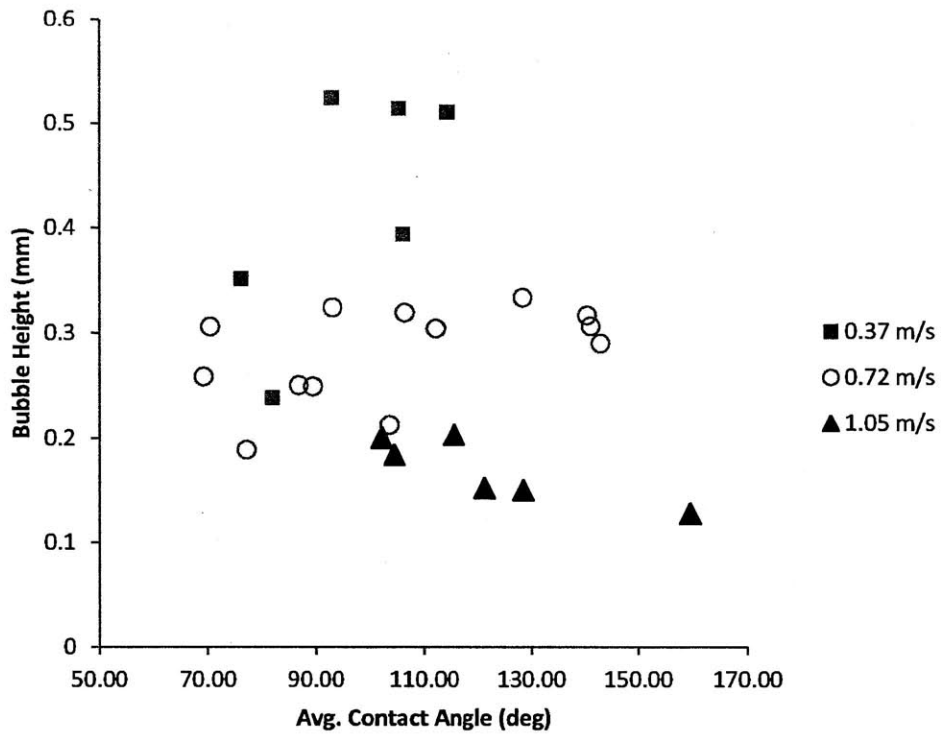


Figure 4.1.11. Bubble height is compared to average contact angle. For each flow rate, bubble height appears to be relatively constant across all contact angles. However, the dependence of height on flow rate is striking. Faster flows clearly lead to shorter bubbles.

According to Figure 4.1.11, bubble height is strongly correlated with flow rate (or flow speed) but shows almost no correlation with contact angle. As with the bubble width, comparing the height to the downstream and upstream contact angles separately yields no new information, but will be included here for completeness. Figure 4.1.12 shows these comparisons.

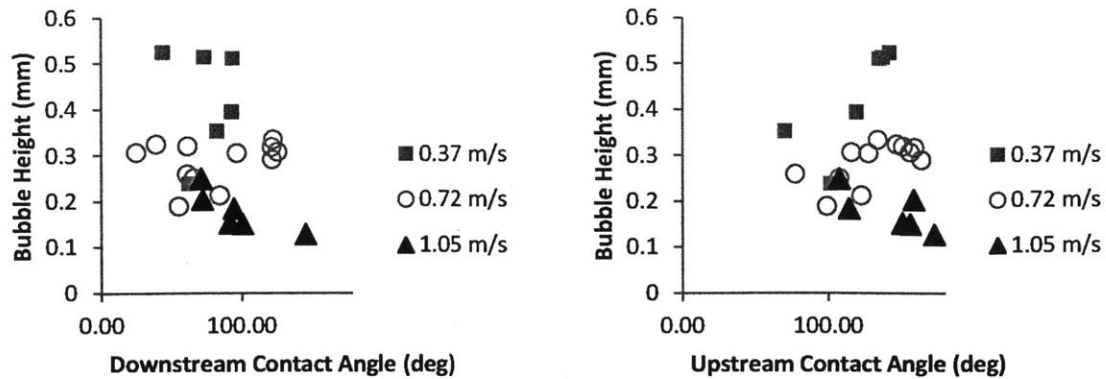


Figure 4.1.12. Bubble height is compared to downstream (at left) and upstream (at right) contact angle to see if the effect of one is greater. These show the same inverse correlation of height with flow rate but all plots show no obvious relationship between bubble height and contact angle.

Comparisons of height to the downstream and upstream contact angles individually show the same inverse correlation of height with flow rate but still show no obvious correlation between bubble height and contact angle. In all likelihood, the relationship to average contact angle is clearer because the wettability is so varied on the surface that the average contact angle was a better predictor of local wettability than either the downstream or upstream contact angles.

Figure 4.1.13 plots height against flow speed without regard to contact angle and shows the inverse correlation.

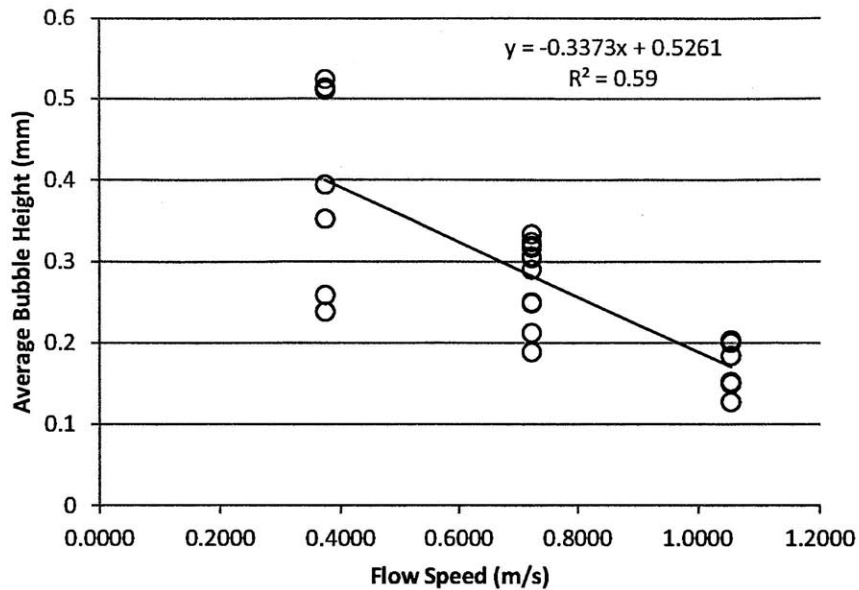


Figure 4.1.13. Bubble height is plotted against flow speed, showing the decreasing relationship.

Height is clearly dependent on flow speed in this experiment: the minimum, maximum, and average height all decrease monotonically with flow speed. The variation in height also appears to decrease with bubble height. There is too much scatter to determine the shape of the correlation, but for a linear fit the bubble height can be estimated to decrease by 0.38 mm per m/s of fluid speed.

By affecting the wettability, contamination increased the bubble sizes at departure over the clean surface. Contamination gave the surface a greater variability in contact angle but on average made the surface more hydrophobic. The contaminated surface had an average contact angle of 106.7° ³ compared to 39.1° for a smooth, plasma-cleaned surface. A first-order approximation which assumes a linear relationship between contact angle and bubble width of 0.01127 mm/degree, as found from the data in Figure 4.1.9, shows that the bubbles on the contaminated surface should be 0.76 mm wider on the contaminated surface than on the equivalent surface without contamination. Given that the average width of all departing bubbles analyzed in this experiment was 0.50 mm, that difference is significant. Clearly the average bubble departing from a smooth, oxygen plasma-cleaned silicon surface would not be negative,

³ Average was calculated from all departing bubbles used in the data analysis, rather than the separate contact angle measurements which were all at the same location.

as the estimated change in width would suggest. There are many variables and uncertainties that limit the usefulness of this estimation, but the point is that the magnitude of the possible change in bubble size due to contamination is significant compared to the magnitude of the bubbles. Therefore, contamination can greatly affect the bubble size in a boiler. Assuming that bubble width (and/or contact angle) has some effect on heat flux, contamination will have a great effect on the performance of a boiler. This effect may be amplified in micro- and nano-structured surfaces, whose usefulness may be compromised by even a small amount of contamination.

A theoretical model was developed relating bubble dimensions at departure to the upstream and downstream contact angles. The contact angles will be extracted from the experimental results to find the theoretical departure size. The theoretical results are calculated from Equations 11 through 13 and are compared to the measured results.

In calculating the theoretical bubble dimensions, the following values of surface tension and density were used. The surface tension of water in contact with air at 100°C is taken to be 0.0598 N/m [7]. This value of surface tension is not entirely accurate for this experiment because of the mix of steam and air in the bubbles and the range of temperatures at which nucleation occurred (see Table 3.3.1), but it will be fairly close to the actual values for the bubbles recorded. The water density, again at 100°C, is taken to be 958.4 kg/m³ [8].

First, the bubble width at departure was evaluated theoretically based on the measured contact angles and the flow speed. The measured and theoretical results for all bubble widths are plotted together in Figure 4.1.14 to show the agreement of the model with the observed behavior.

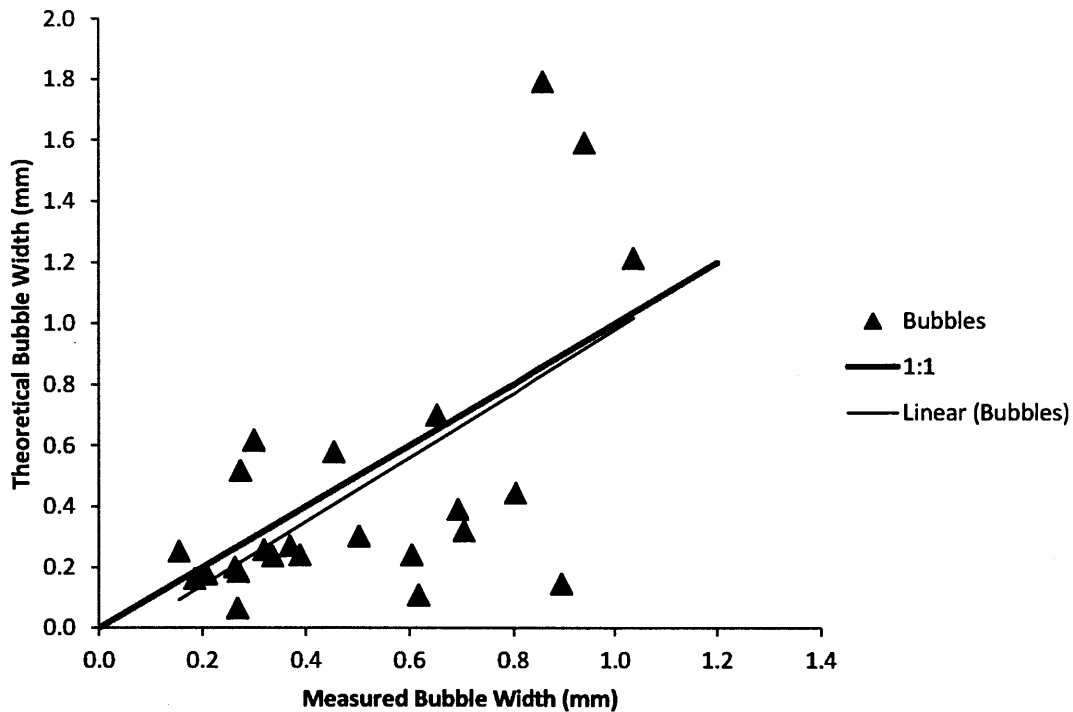


Figure 4.1.14. Theoretical bubble width is compared to the data. The theoretical width is based on the measured upstream and downstream angles of the bubbles recorded at departure. Though there is a lot of scatter, the linear fit of the model versus the data is very close to the 1:1 line, showing a reasonable level of agreement between the model and the data.

The theoretical model generally predicts the measured bubble width well, though there is a lot of scatter. A linear fit of the theoretical to the measured bubble width almost exactly matches the 1:1 line drawn between the model and data. This is good, but the scatter indicates that for a given bubble, the model will not necessarily predict the width at departure with accuracy. This suggests that there are factors excluded by the model that affect the bubble width at departure. One bubble was excluded from the plots in Figures 4.1.14 and 4.1.15 which had an upstream contact angle greater than its downstream contact angle, leading to negative theoretical width and height.

The bubble height at departure was also predicted theoretically for the measured contact angles. This comparison, which shows a more marked discrepancy between the model and data, is shown in Figure 4.1.15, below.

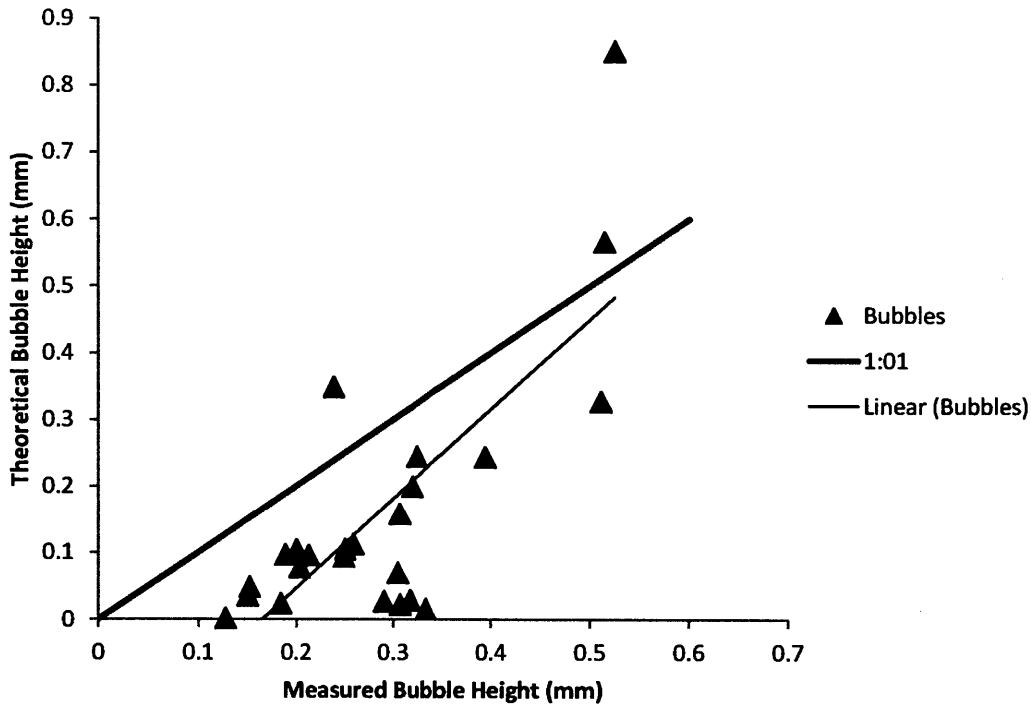


Figure 4.1.15. Theoretical bubble height is compared to the data. The agreement is fairly good though there is a shift of about 0.15 mm between the measured and theoretical bubble height, with the theory predicting shorter bubbles than were actually observed. This is probably due to the assumption that each bubble was a skewed truncated sphere, a shape which did not always accurately describe the bubbles observed.

The theoretical and measured bubble height appear to be better correlated than the theoretical and measured bubble width, but there is a clear shift between the two values. The measured bubble height seems to be about 0.15 mm larger than that predicted by the model. This is likely to be due to the assumption that the bubbles are skewed⁴ truncated spheres. The projected area in the plane of the images captured would then be a skewed truncated circle, but this is generally not the case. In almost all cases, the bubble was taller than it would have been if it had formed a truncated circle between the two points of contact with the same contact angles.

⁴ Skewing a sphere (in this case, in the direction of flow) affects neither its volume nor its projected area perpendicular to the direction of flow.

Figure 4.1.16 shows two examples of real bubbles overlaid with skewed circles to show the discrepancy.

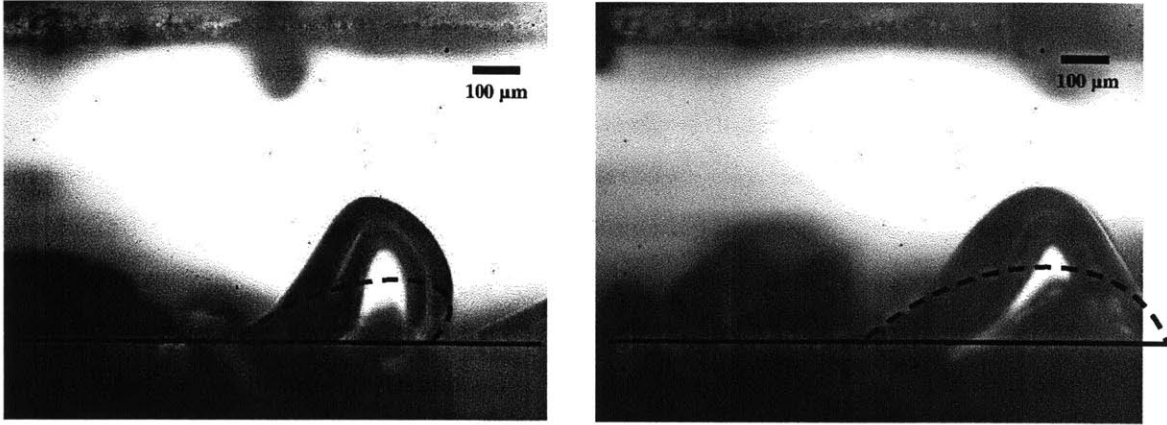


Figure 4.1.16. Two bubbles at the moment before departure with overlays of the assumed bubble shape shown by a dotted line. Bubbles were assumed to be skewed truncated spheres with a truncated skewed circle for a cross section. In both cases, as it seems to be in all images taken of bubbles the moment before departure, the bubble is taller than would be predicted by the truncated skewed sphere model.

Bubbles were assumed to be skewed truncated spheres, with the cross section in the plane of the video being a truncated skewed circle. In almost all (or perhaps all) images taken of bubbles the moment before departure, the bubble was taller than would be predicted by the truncated skewed sphere model. This helps explain the discrepancy between the measured and theoretical data, in which the measured height is generally greater than the predicted height.

Deviations of the model from the data may originate from several other assumptions that are not entirely accurate. Assuming that the liquid behind the bubble lost all x-direction velocity, neglecting shear, and neglecting pressure changes between the bulk fluid and the fluid in contact with the bubble is inaccurate, and should be replaced by a drag force that depends on the size and shape of the bubble and the velocity profile in the channel. Additionally, it was assumed that departure is governed by an imbalance in forces in the flow direction, but it is possible that for some bubbles departure was triggered by forces in the direction normal to the surface. Employing a drag force and determining whether and when bubbles depart due to a force imbalance in the direction normal to the surface will improve the model. Additionally, the

surface tension force term assumes that the contact angle is equal to the upstream and downstream contact angles on one half of the contact line each. Generally the contact angle will vary smoothly around the contact line. In this experiment, the equilibrium contact angle was widely varied over the surface, making the assumption of binary contact angles even less accurate. Further study into bubble shapes in flow and comparison with data from a better-controlled experiment will lead to a model with better agreement to the data.

Despite the areas for improvement in the current model, the theory explains the data well enough that the parameters in the theoretical bubble size correlations should be considered when designing surfaces. The width and height depend on the advancing and receding contact angles and the flow speed. If the ideal surface would have departure occurring when bubbles are as small as possible, both width and height should be minimized. Looking back at Equations 11 and 13, this would mean that increased water velocity, decreased contact angle hysteresis⁵, and decreased equilibrium contact angle all contribute to smaller departing bubbles. There are also minor effects related to the equilibrium contact angle that will affect the departure size. Further research or literature review are needed to determine the factors affecting contact angle hysteresis. Decreasing the surface tension of the water by the addition of a surfactant could also decrease bubble size.

If bubbles should be made tall and thin (with large height but small width), the ideal surface and flow parameters are more difficult to quantify. Equation 13 shows that to maximize H/W , the factor $(1+\cos\theta_a)/\sin\theta_a$ should be maximized. If tall, thin bubbles are found to be beneficial, a numerical study should be undertaken to find the optimal surface and flow parameters.

A study of the true shapes taken by bubbles in flow boiling should be undertaken to find a more accurate geometrical basis for the theoretical bubble size predictions. This will enable more accurate prediction of bubble height which can then be used to find departing bubble volume.

⁵ Really, it is $\cos\theta_d - \cos\theta_a$ that should be minimized, but for contact angles near 90° , $\cos\theta \approx (\pi/2 - \theta)$ so that $\cos\theta_d - \cos\theta_a \approx \theta_a - \theta_d = 2\Delta\theta$.

4.2 Observations

During the course of this experiment I had the chance to watch many bubbles form and depart and observe their behavior. High-speed video would enhance understanding of bubble behaviors and departure dynamics, but even the 30 fps video recorded in this experiment shows some interesting phenomena.

Just before departure, bubbles sometimes exhibited wiggling behavior, as shown by the bubble in Figure 4.2.1.

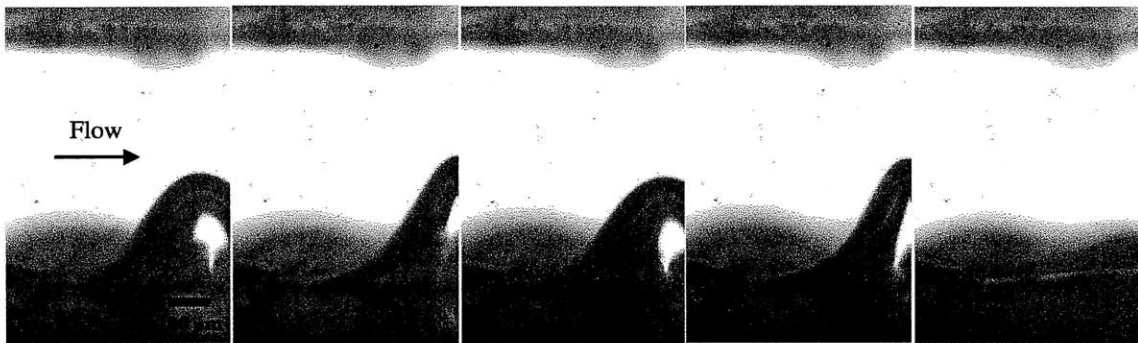


Figure 4.2.1. A bubble wiggling before departure. In this figure, time progresses to the right in 33.3 ms increments.

The bubble in Figure 4.2.1 (which was cut off by the frame of the video) wiggles back and forth at least a few times. The frequency of wiggling must be a multiple of half the video frame rate for the wiggling to show so clearly in the video. Many bubbles did not appear to wiggle with such high amplitude. There was some oscillation of flow rate due to the peristaltic pump, though this oscillation was relatively small—around $1/10^{\text{th}}$ the average flow rate or smaller. If bubbles were to have some resonant frequency of oscillation at departure, the oscillation of the flow (due either to the peristaltic pump or flow instability) could set the bubble oscillating at its resonant frequency and cause it to depart. Other bubbles may have had different resonant frequencies at departure, and either did not match the frequency of oscillation of the flow or did resonate but it was not clear in the video due to the mismatch between the resonant frequency and the frame rate. Finally, it is possible that there is no such thing as a bubble resonant frequency or that it does not lead to departure. Observation of bubbles with very high

speed video would answer this question, and is worthwhile because a discovery of this nature could possibly lead to the design of boiling systems which purposefully oscillate the flow to trigger departure of bubbles of a certain size.

Another departing bubble that rapidly changes shape before departure is shown in Figure 4.2.2.

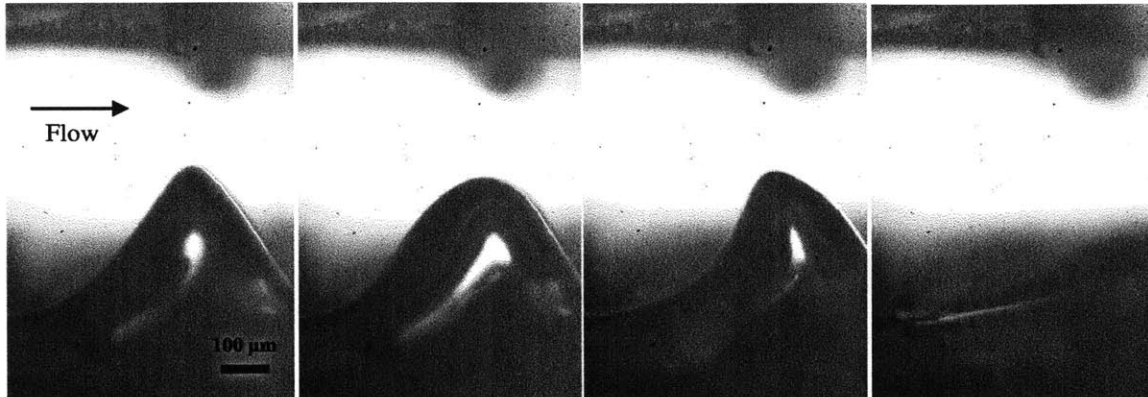


Figure 4.2.2. A bubble changing shape rapidly before departure. Time progresses to the right in 33.3 ms increments. After some time in the triangular shape shown in the leftmost image, the bubble gets rounder, stretches back into a triangle which briefly points upstream, and then departs.

The bubble in Figure 4.2.2 rapidly changes shape before departure. After some time in the triangular shape shown in the leftmost image, the bubble gets rounder, stretches back into a triangle which points upstream, and then departs. Again, it is hard to see exactly what is happening due to the 30 fps frame rate, but the onset of rapid changes of shape is likely to have some relationship to the bubble's departure. It is unclear whether a bubble that is about to depart is susceptible to rapid changes of shape or whether some external factor causes these changes of shape which in turn put forces on the bubble that cause it to depart.

The initial shape of the bubble in Figure 4.2.2 (above) also merits discussion. Bubbles tend to form round shapes in order to minimize surface energy, so the triangular shape is unusual. Figure 4.2.3 shows another triangular bubble at the moment before departure.

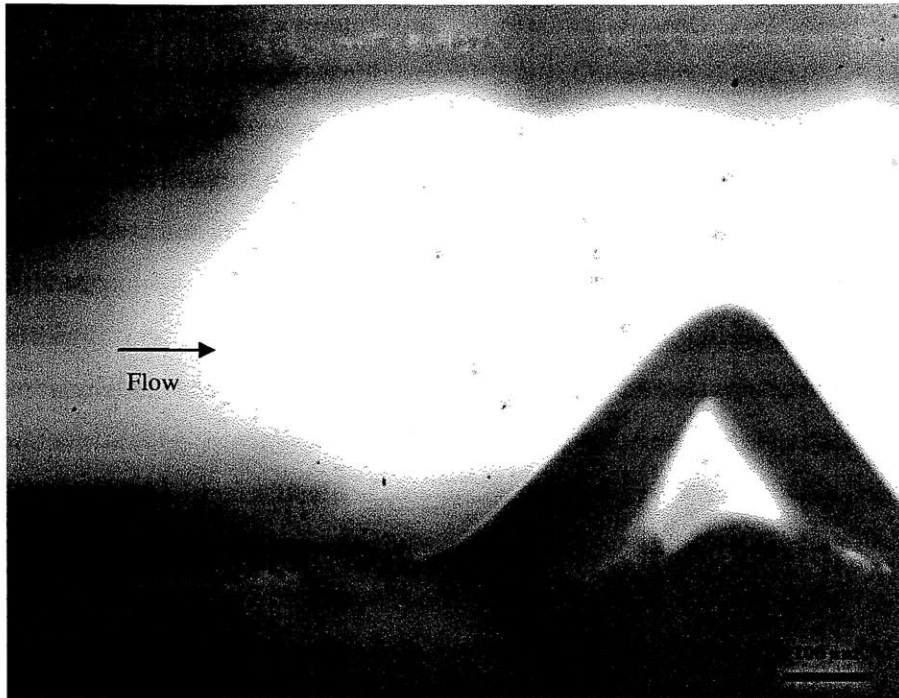


Figure 4.2.3. A triangular bubble in 0.72 m/s flow at the moment before departure.

Figure 4.2.3 shows a triangle-shaped bubble in 0.72 m/s flow at the moment before departure. The non-round shape does little to minimize surface area, and thus is likely to have higher surface energy than a more typical round bubble. However, this shape could possibly minimize surface energy if the bubble were pinned to something above or below the plane of the video. Unfortunately there is no record of the bubble's shape at other planes. The front and back of the channel are far enough from the bubble (around 2 mm on each side of the video plane) that pinning to these planes is unlikely assuming a bubble depth similar to its width, around 0.7 mm. It is also conceivable that the shape is strange because surface tension forces are not dominant. If other forces such as stagnation pressure or shear from the flow of the water around the bubble were dominant, it is not inconceivable that a triangle could be a natural bubbles shape. Finally, the footprint of the bubble may be unusual due to the rapidly-varying wettability of the surface. A bubble that takes a strange base shape to avoid hydrophilic regions might have an unusual body shape.

The bubble behavior in this experiment was consistent with expectations for a surface of highly-variable wettability, exhibiting rapid changes in shape when skipping over hydrophilic regions. Figure 4.2.4 shows a bubble navigating the variable-wettability surface.

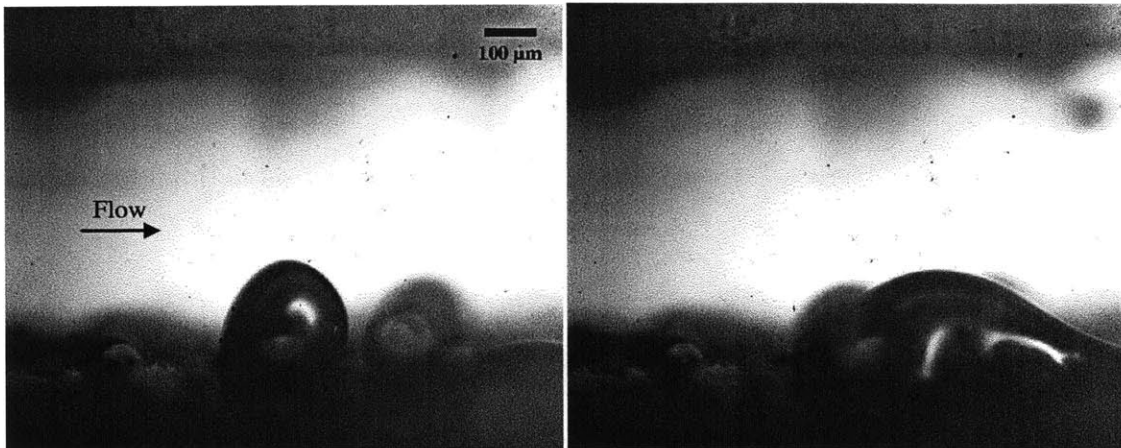


Figure 4.2.4. Two images of the same bubble taken 33.3 ms apart, showing a rapid change in shape when jumping over a hydrophilic region to the next hydrophobic region.

Figure 4.2.4 shows two consecutive stills of a bubble rapidly changing shape. The width, height, and both contact angles change significantly in less than $1/30^{\text{th}}$ of a second. This jump probably occurs due to the presence of a hydrophilic region in front of the bubble (before the shape change) followed by another hydrophobic region. The bubble does not have enough energy to expand into the hydrophilic region so it stays pinned in place, gaining energy in the form of surface tension. Finally, when it has enough energy to remove the water from the hydrophilic region in front of it, it moves forward. When it encounters a drop in wettability, it continues to move forward until it reaches a new equilibrium shape.

An area for future research inspired by this bubble behavior might be the design and testing of surfaces with purposeful, periodic variation in wettability. For instance, by surrounding small areas of superhydrophobicity with a larger superhydrophilic surface, bubbles could be confined to certain areas and small departure sizes while being prevented from contacting one another and forming a film. This might work for pool boiling and well as film boiling, though the design parameters would be different for these two cases. The high variation in wettability could be accomplished through the use of micro- or nano-scale surface textures applied through thin film manufacturing processes. An example of such a surface and its possible effects is shown in Figure 4.2.5.

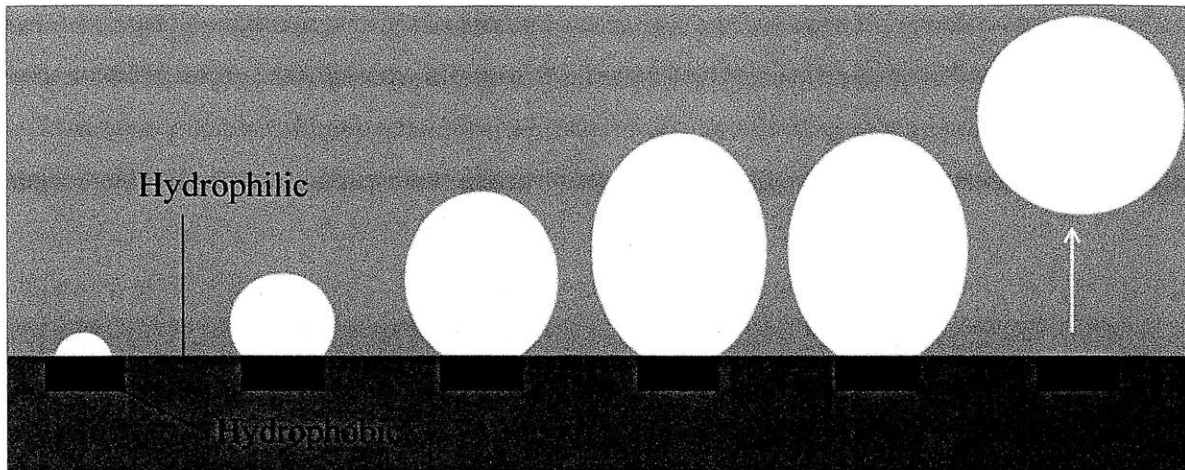


Figure 4.2.5. A hypothetical surface with periodic variations in wettability and the bubble behavior that might be provoked by such a surface, with bubble growth depicted from left to right. Such a surface, designed around an understanding of the bubble's size and shape and departure, could potentially prevent bubbles from coalescing and increase the CHF in pool boiling or increase heat fluxes in flow boiling.

The surface depicted above involves periodically arranged superhydrophobic patches surrounded by a superhydrophilic surface. The surface would have to be designed around an understanding of the shape and size of bubbles at departure for the expected boiling conditions. Hydrophobic regions will encourage rapid bubble nucleation and the hydrophilic portion of the surface will seek contact with the water and increase heat transfer by conduction. This will create tall, narrow bubbles that depart before they coalesce into a film. An example of a tall bubble that is probably trapped in a hydrophobic region between hydrophilic regions is the skinny bubble shown in Figure 4.2.6 below.



Figure 4.2.6. An unusually-shaped bubble that may be trapped in a small hydrophobic area within a hydrophilic region. This surface feature produces a tall, thin bubble that has a small contact area with the surface.

Such a surface could prevent bubbles from coalescing and forming a film and either increase the CHF in pool boiling or increase the heat transfer rate for a given quality and wall temperature in flow boiling. Other factors, such as the conduction resistance through the surface to get between the regions of different local heat fluxes, might make this surface not useful, but it seems promising enough to merit an investigation.

4.3 Evaluation of Experimental Fixture

The experimental fixture needs to be modified if more quantitative experimental results are desired. The apparatus is fine as it is for exploratory studies such as this one, but further study of flow boiling will require better video and heat flux and temperature measurements.

The video quality was mixed. Sometimes the experimental setup produced crisp, clear video. Figure 4.3.1 shows two very clear images where the channel walls are clear and the bubble size and contact angles are easily seen and measured.

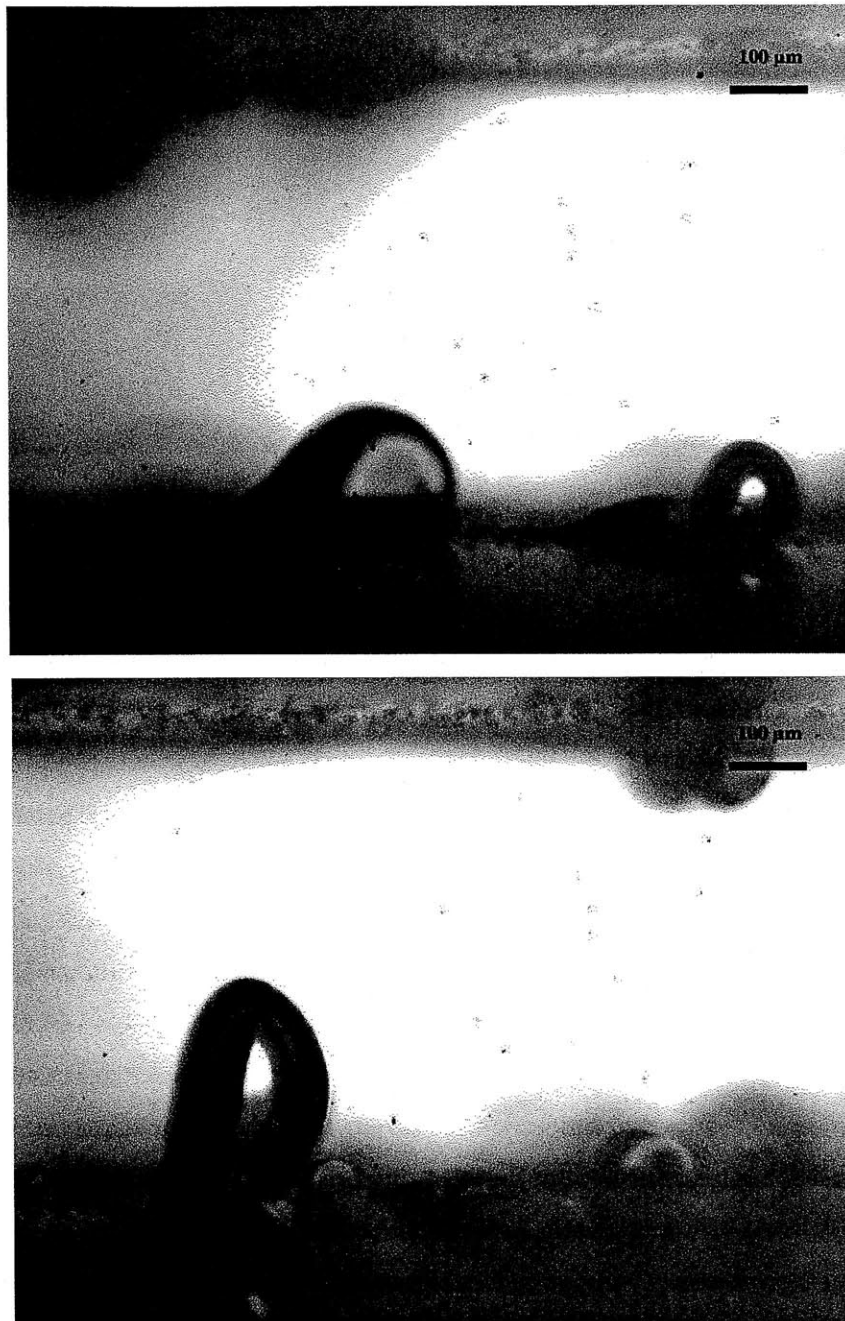


Figure 4.3.1. Two examples of very clear video stills. The bubble width and height, both contact angles, and the channel width are all very clear.

These legible pictures occurred occasionally, and images from which the size and contact angle could be deduced from careful inspection occurred relatively often—about once for every two minutes of video. However, with the amount of time involved in capturing, compiling, and

sifting through the video, this rate of capture of useful pictures was disappointing and shows room for improvement.

Several conditions led to poor picture quality. Figure 4.3.2 shows two common types of visual interference that rendered the video of many departing bubbles unusable.



Figure 4.3.2. Two examples of unclear video stills. Many bubble departure stills could not be used because the points of contact with the surface were obscured by other bubbles or due to lack of contrast with the back of the channel. In other instances a departing bubble would be partially cut off by the frame of the video.

As shown above, any bubble departure stills could not be used because the points of contact with the surface were obscured by other bubbles or due to lack of contrast with the back of the channel. The contrast varied throughout the channel because the spacer wafer that held the two sides of the channel apart was not cut cleanly and the edges were slightly uneven. Fixing the channel spacer such that it had a perpendicular edge with a mirror finish would greatly help the image quality by reflecting the light from the microscope back through the bubbles. The bubbles will appear dark on the edges because the angle of the light on the bubble surface will exceed the critical angle for transmission of light from a high refractive index material (in this case, water) to a low one.

In other instances departing bubbles are partially cut off by the frame of the video. When this happened, dimensional data was only collected from such bubbles images whenever the portion cut off was small enough that the width and contact angle could be reasonably estimated.

Even in pictures where nothing was cut off, estimating the contact angle was still more of an art than a science. The MATLAB script for measurement of dimensions repeated the cycle of clicks three times to reduce error, but the variation in contact angle was on the order of a few degrees between the different cycles of clicks during test runs where each cycle was analyzed individually. Therefore the uncertainty in contact angle measurement due to errors in clicking is likely to be around 1-2°, with another few degrees of contact angle uncertainty due to the images being unclear. For a qualitative paper such as this one this uncertainty is small enough, but for more precise research image clarity needs to be improved and data should be collected through a more refined method of image processing. Other dimensions such as the width and the channel height are likely to be accurate to within a few pixels, or around 10 microns.⁶

Further uncertainties are introduced by the lack of time-resolution in the video. Due to the great length of time involved in compiling the video files and the great length of video necessary to get each image of a bubble's departure, the frame rate of 30 frames per second was chosen. In this experiment, the bubbles grew so slowly that the change in bubble size within the (at most) 1/30th of a second between the last picture taken of a bubble and its departure was not significant, especially compared to the shifts in shape and size due to fluctuations in channel pressure and flow speed due to the peristaltic pump and the behavior of other bubbles. However, the exact departure dynamics of the bubbles in this experiment are unknown due to the low frame rate. Figure 4.3.3 shows the before and after shots of a bubble departure to illustrate how little can be determined from non-high-speed video of bubbles in such a high-speed⁷ flow.

⁶ Estimated from the variation in the measured channel widths of all images from the 0.72 m/s flow boiling video.

⁷ For reference, the water flows through on the order of 25 frame-widths of the channel per frame in the video.

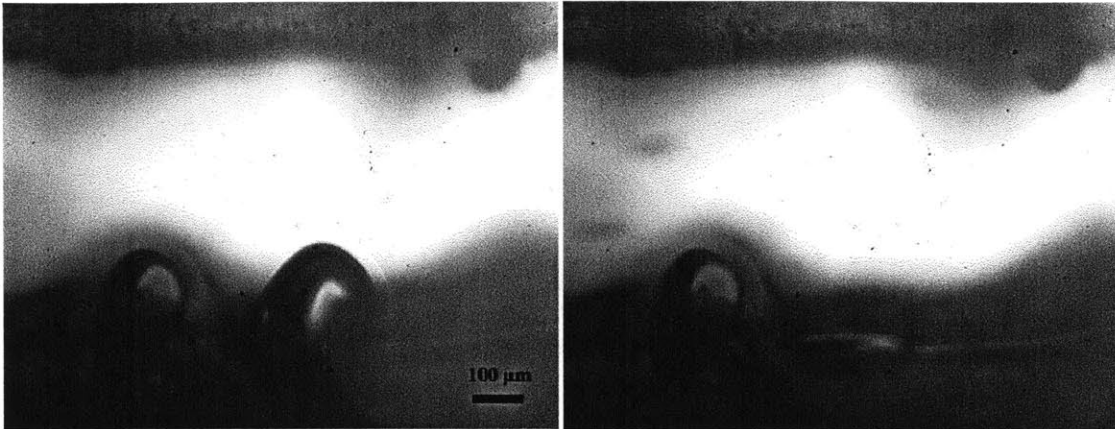


Figure 4.3.3. Consecutive images of a departing bubble, showing that video frame rate should be increased if a better understanding of departure dynamics is desired.

Given the time constraints of this experiment, such a low frame rate was necessary, but in future experiments on bubble departure dynamics, high-speed video should be used. In order to capture the bubble's departure, one or more images should be captured in each time interval necessary for an element of water at the average flow speed to travel from one end of the frame to the other. This will be more time-consuming per bubble filmed, but by eliminating contamination in the fixture, uniform surfaces with repeatable bubble departures can be used so that only a few bubbles must be recorded to develop a good understanding of the subcooled nucleate boiling regime of flow boiling.

Eliminating contamination will be difficult, but even reducing the contamination to a level where wafers of different contact angles can be used for a short time without significant changes in wettability has proven difficult. Flushing the system with deionized water and cleaning the metal preheater with hydrochloric acid was fruitless. The contaminated section of wafer, which was the part in contact with the water in the channel, appears to be coated with a whitish powder, as shown in Figure 4.3.4.

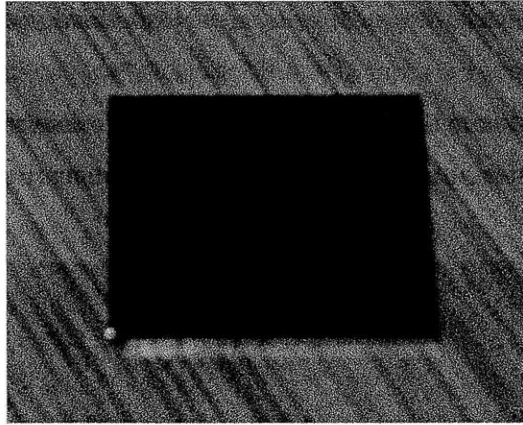


Figure 4.3.4. Used plain silicon surface showing visual evidence of contamination on the right side where the water contacts the surface.

As shown in Figure 4.3.3, the portion of the surface which is in contact with the water in the channel is coated with a whitish powdery substance. This changes both the composition and the structure of the surface, resulting in a decrease in wettability (on average) and an increase in the variability of the equilibrium contact angle.

To find the source of the contamination, an X-ray photoelectron spectroscopy test was conducted on the contaminated portion of the wafer to determine the chemical composition of the contamination.⁸ The results are presented in Figure 4.3.5.

⁸ Siyu Chen took the surface for testing.

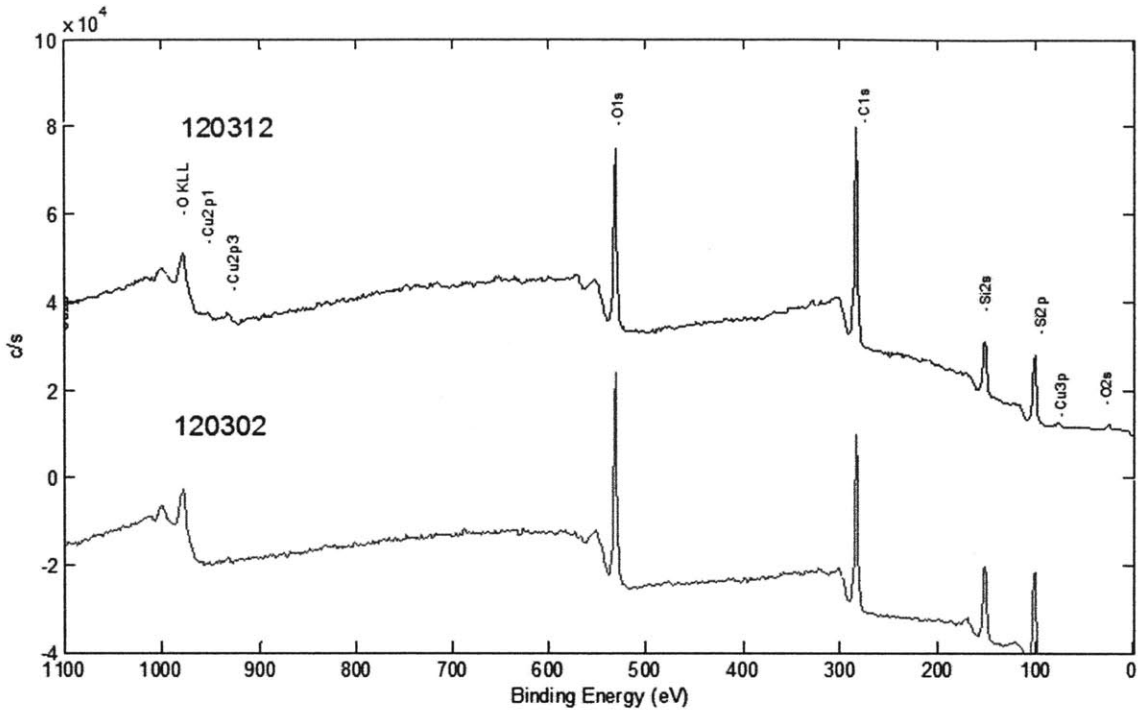


Figure 4.3.5. An X-ray photoelectron spectroscopy (XPS) test of the contaminated wafer surface. Large peaks indicate the presence of oxygen and carbon.

The largest peaks are at oxygen and carbon, indicating oxygen and carbon contamination. One of the silicon peaks is slightly shifted, which could point to the presence of silicone or silicate. There are silicone components of the fixture (both tubing and RTV sealant) but silicone is fairly unlikely to diffuse into water, and the shift in the silicone peak may not be meaningful. The oxygen probably came from the silicon dioxide that forms on the surface during the oxygen plasma cleaning, but the carbon is concerning. Many of the fixture components are hydrocarbon based (mostly plastics) and any of them could contribute carbon contamination. If this fixture is going to be used for future boiling experiments the component(s) producing the contamination will need to be identified and replaced, especially for testing microstructured or nanostructured surfaces.

It would be useful to be able to measure pressures in the system, including both the absolute pressure of the channel and the pressure drop through the channel. The absolute pressure could be used to determine the saturation temperature and thereby the air and steam content of the bubbles based on the temperature at which bubbles begin to nucleate on the

surface. The differential pressure measurement across the channel could be used to estimate the forces on the bubbles and measure the flow instability due to boiling in the channel. At present, pressure measurement is difficult due to the tendency of bubbles in the channel to enter the lines to the pressure transducer. In steady-state, the air bubbles in the lines will not affect the measured pressure, but at a short time scale the bubbles will dampen the response of the pressure transducer to rapid fluctuations in pressure drop in the channel due to flow instability. Also, eddies are likely to form in the regions near the openings to the pressure transducer (see Figure 3.1.3) which may introduce error into the pressure measurement.

Finally, most experiments that test boiling on surfaces of interest measure the surface temperature and heat flux in order to construct a boiling curve for the surface-fluid combination. The current experimental apparatus is not well set up for surface temperature or heat flux measurement. A new fixture should be designed for the testing of future surfaces. Many of the components can be reused. Thermocouples should be integrated into the surface for accurate temperature measurement. A heater should be used that is either very well insulated so that the power and area of heat flux can be known or contains a built-in heat flux sensor such as a series of thermocouples measuring the temperature drop across a region of known thermal conductance which can be used to determine the heat flux. Constructing boiling curves for flow boiling at different qualities could lead to new insights about boiler design.

5. CONCLUSION

This research found the parameters affecting subcooled nucleate flow boiling based on the bubble width and height at departure with moderate success. Contamination in the fixture and variable video quality increased the scatter in the results, but the contamination also allowed for the use of a variable-wettability surface, which enabled the correlation of bubble width and height at departure to the upstream and downstream contact angles. Theory was developed in parallel to inform the design of surfaces in boiling.

The experimental results show some scatter, but several trends emerged. It is clear that the bubble width increases with equilibrium contact angle and decreases with flow speed. Bubble height is shown to decrease with flow speed, but shows little relationship to contact angle in the experimental data.

The theoretical predictions of bubble size give further insight into the parameters controlling bubble departure. The agreement between the theory and data is by no means perfect, but is good enough that some aspects of the theoretical predictions can be used to inform the design of surfaces for flow boiling. The model developed indicates that both width and height decrease with flow speed and increase with equilibrium contact angle and the amount of contact angle hysteresis. With future modifications to the model to account for the deviations of the bubbles from the assumed geometry and research into the parameters controlling contact angle hysteresis of bubbles in flow, these theoretical correlations will inform the design of surfaces and flow parameters for increasing heat transfer coefficients in flow boiling.

In the future, more research should be done in several related areas. A new fixture should be constructed, free of contamination, which can measure the surface temperature and heat flux while still collecting side-on bubble video. This will help determine the relationship between of bubble size and shape at departure to the heat transfer coefficient for a given quality. Surfaces should be tested that span the range of wettability, and in the limit of complete wetting, also span a range of surface roughness to determine the additional effects of roughness on bubble departure. Mixed-wettability surfaces with periodically-varying contact angle (and, perhaps, roughness) should be explored which control the size, shape and spacing of bubbles to prevent film formation and potentially increase the heat transfer coefficients in flow boiling or the CHF in pool boiling. The model of bubble departure developed here should be modified to more

accurately reflect the geometry of bubbles in flow as well as be able to predict the upstream and downstream contact angles based on surface and flow parameters and to be able to handle bubbles resting on interfaces between regions of different wettability.

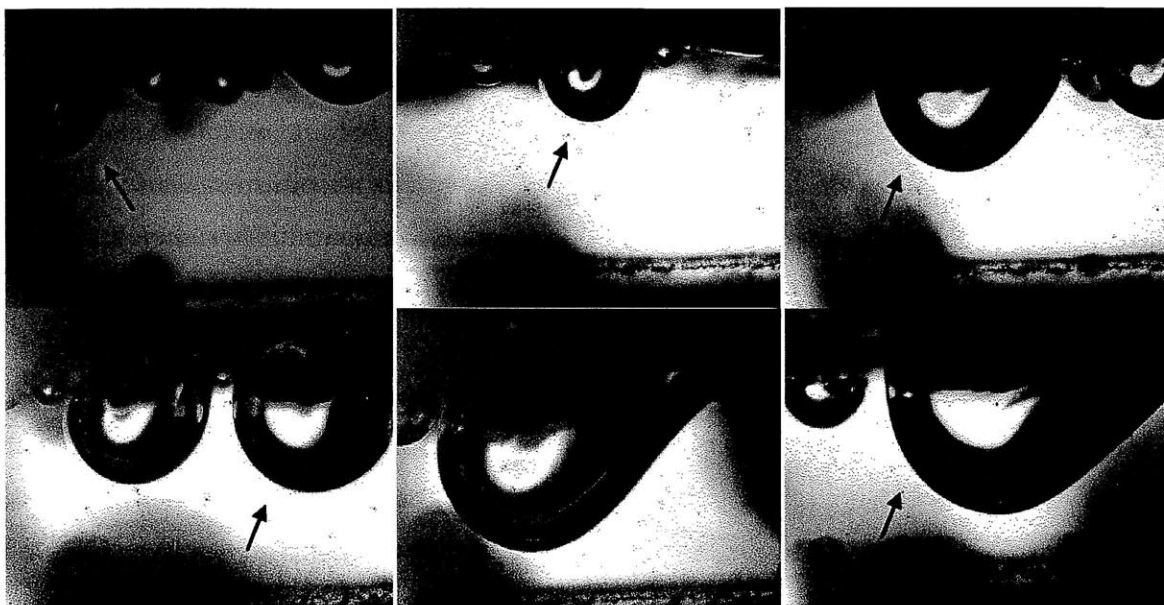
6. REFERENCES

- [1] G. E. Moore, "Cramming more components onto integrated circuits", *Electronics*, 38.8, 1965.
- [2] Chu, K., Enright, R, Wang, E. N., "Microstructured surfaces for enhanced pool boiling heat transfer," Proceedings of the ASME 2011 International Mechanical Engineering Congress & Exposition, November 11-17, 2011.
- [3] S. S. Kutateladze, "On the transition to film boiling under natural convection," *Kotloturbostroenie*, 3, 10–12, 1948.
- [4] J. H. Lienhard IV, J. H. Lienhard V, *A Heat Transfer Textbook*, 4 ed. Cambridge, MA: Philogiston Press, 2011, 499.
- [5] R. Tadmor, "Line energy and the relation between advancing, receding, and young contact angles," *The ACS Journal Surfaces and Colloids*, 20, 18, 7659-64, 2004.
- [6] S. G. Kandlikar, B. J. Stumm, " A Control Volume Approach for Investigating Forces on a Departing Bubble Under Subcooled Flow Boiling," *Journal of Heat Transfer*, 117, 4, 990-7, Nov. 1995.
- [7] "Surface Tension of Water in contact with Air," Engineering Toolbox. [Web]. Available: http://www.engineeringtoolbox.com/water-surface-tension-d_597.html. [Accessed: 4/26/12].
- [8] "Water: Density and Specific Weight," Engineering Toolbox. [Web]. Available: http://www.engineeringtoolbox.com/water-density-specific-weight-d_595.html [Accessed: 4/26/12].

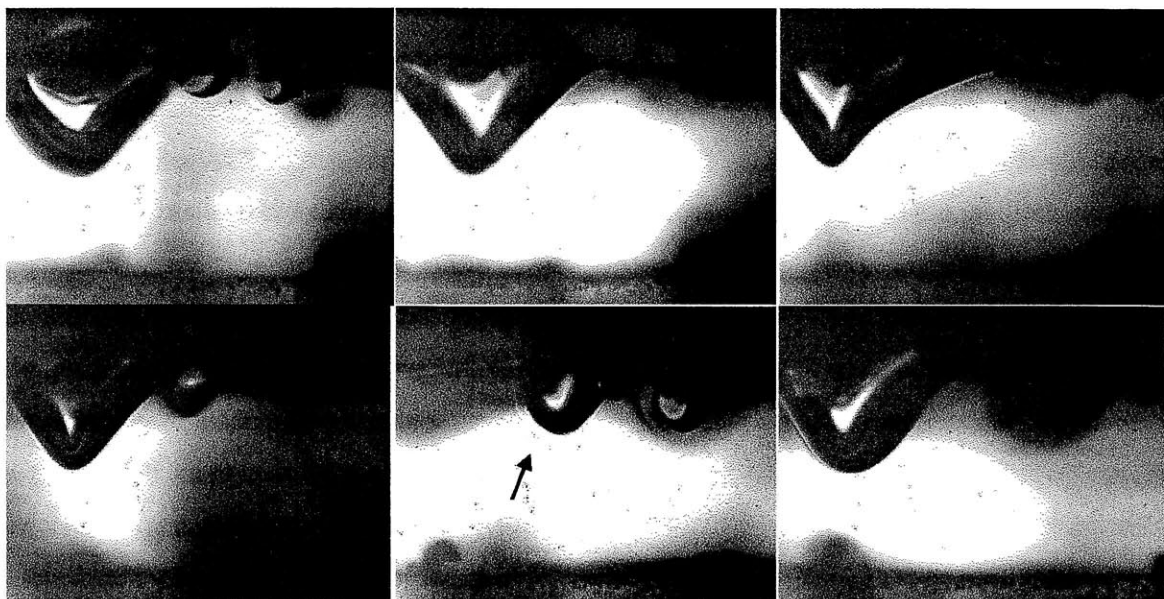
APPENDIX I: All Departing Bubbles on Contaminated Surface

Note: arrows indicate departing bubble when multiple bubbles are present. As a dimensional reference, the channel width (easily seen in all images) is 0.67 mm.

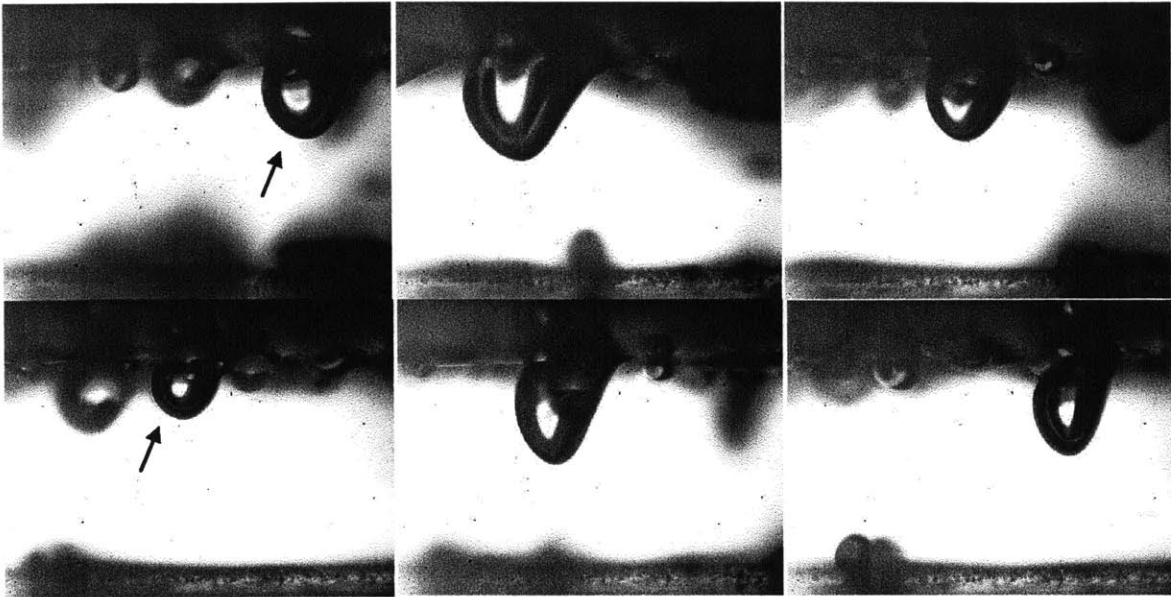
0.37 m/s (6 images)



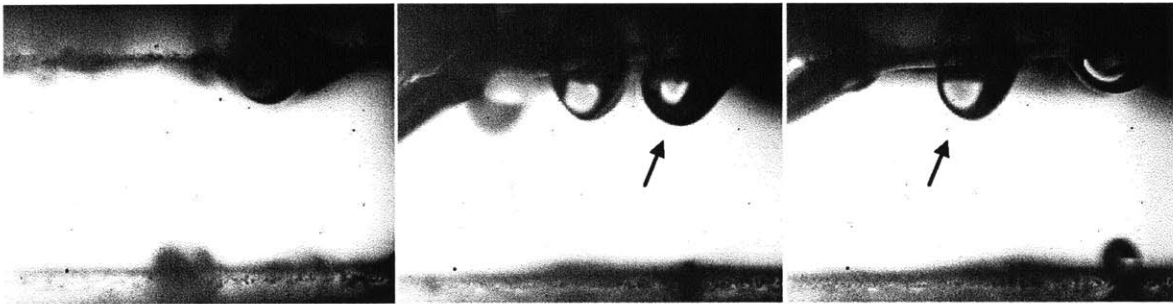
0.72 m/s (12 images)



0.72 m/s, continued



1.05 m/s (7 images)



1.05 m/s (continued)



APPENDIX II: Image processing MATLAB scripts

Note: Before running scripts, first open image with *imshow*.

1. Channel height, bubble width, and contact angles

```
[x,y]=ginput(21); %do 3 cycles

%average
x=(x(1:7)+x(8:14)+x(15:21))/3;
y=(y(1:7)+y(8:14)+y(15:21))/3;

%get coordinate system
ax=x(1)-x(2);
ay=y(1)-y(2);
bx=x(3)-x(2);
by=y(3)-y(2);
channel_D=abs(ax*by-ay*bx)/sqrt(ax^2+ay^2); %cross product

%get bubble width
width=sqrt((x(6)-x(4))^2+(y(6)-y(4))^2);

%get contact angles
cx=x(5)-x(4);
cy=y(5)-y(4);
dx=x(7)-x(6);
dy=y(7)-y(6);
theta_r=pi-acos((ax*cx+ay*cy)/(sqrt(ax^2+ay^2)*sqrt(cx^2+cy^2)));
theta_a=acos((ax*dx+ay*dy)/(sqrt(ax^2+ay^2)*sqrt(dx^2+dy^2)));

%output
W_TA_TB_CD=[width theta_a theta_r channel_D]
```

2. Bubble height

```
[x,y]=ginput(9); %do 3 cycles

%average
x=(x(1:3)+x(4:6)+x(7:9))/3;
y=(y(1:3)+y(4:6)+y(7:9))/3;

ax=x(2)-x(1);
ay=y(2)-y(1);
bx=x(3)-x(1);
by=y(3)-y(1);
H=abs(ax*by-ay*bx)/sqrt(ax^2+ay^2) %cross product
```